Chemical Science

ROYAL SOCIETY OF CHEMISTRY

REVIEW

View Article Online
View Journal | View Issue

Cite this: *Chem. Sci.*, 2025, **16**, 21677

Can single-atom precision rewire the electrochemical logic of Li–S chemistry? A comprehensive review of single-atom catalysts as agents of precise modulation

Yue Wang, †[a] Haobin Song,†[ab] Nan Zhao,†[ab] Xi Cheng,[c] Dong-Sheng Li [d] and Hui Ying Yang *[a]

Single-atom catalysts (SACs) present a compelling strategy to overcome the persistent challenges in lithium–sulfur batteries, such as polysulfide shuttling and sluggish redox kinetics. Their atomically dispersed nature and tunable coordination structures enable selective modulation of intermediate species and catalytic interfaces. Despite rapid progress, SAC design remains largely empirical, lacking a unified mechanistic framework. In this review, we outline a precision catalysis paradigm for SACs in lithium–sulfur systems. The discussion is organized along three core dimensions: spatial configuration, reaction pathway control, and functional integration. We summarize how coordination asymmetry, charge redistribution, and interfacial electronic coupling influence the adsorption and transformation of lithium polysulfides and Li_2S. These insights are supported by spectroscopic characterization and theoretical calculations. Beyond conventional activity descriptors, we uncover structure–activity correlations involving d-band shifts, orbital hybridization, and electronic field effects. The concluded framework is further applied to sodium–sulfur, potassium–sulfur, and solid-state lithium–sulfur systems, demonstrating broad applicability. This review advances the understanding of SACs from passive

Received 30th July 2025
Accepted 12th October 2025

DOI: 10.1039/d5sc05720e

rsc.li/chemical-science

[a]*Department of Materials Science and Engineering, College of Design and Engineering, National University of Singapore, 9 Engineering Drive 1, Singapore 117575, Singapore. E-mail: yanghuiying@nus.edu.sg*

[b]*Pillar of Engineering Product Development, Singapore University of Technology and Design, 8 Somapah Road, Singapore 487372, Singapore*

[c]*The UWCSEA Dover Campus, 1207 Dover Road, Singapore 139654, Singapore*

[d]*College of Materials and Chemical Engineering, Key Laboratory of Inorganic Nonmetallic Crystalline and Energy Conversion Materials, China Three Gorges University, Yichang 443002, China*

† These authors contributed equally.

Wang Yue

Yue Wang is a research fellow in Professor Hui Ying Yang's group at the National University of Singapore. He received his Ph.D. in Materials Science from Nanjing University and previously worked at the Singapore University of Technology and Design. His research lies in electrochemical energy storage, with particular focus on sodium- and potassium-ion batteries, sodium–sulfur chemistry, and solid-state sodium–sulfur batteries. He has published in journals including Advanced Materials, Angewandte Chemie International Edition, ACS Nano, and Energy & Environmental Science, contributing theoretical and experimental insights toward next-generation energy devices.

Hui Ying Yang

Hui Ying Yang is a Professor in the Department of Materials Science and Engineering at the National University of Singapore. She received her Ph.D. from Nanyang Technological University and previously held faculty appointments at the Singapore University of Technology and Design and visiting assistant professor at the Massachusetts Institute of Technology. Her research focuses on advanced nanomaterials for energy storage and water treatment, leading to over 400 publications with more than 30 000 citations (H-index 100) and international recognition including the NRF Investigatorship and ACS Nano Impact Award.

adsorption sites toward programmable redox regulation. It provides conceptual and design guidance for future catalyst development based on adaptive coordination environments and data-driven optimization strategies.

1. Introduction

Lithium–sulfur (Li–S) batteries represent a pivotal direction for next-generation energy storage, boasting exceptional theoretical capacity (1675 mA h g^{-1}), outstanding energy density (approximately 2600 W h kg^{-1}), and sulfur's natural abundance.[1–5] Nevertheless, their practical implementation faces three intertwined challenges: (i) the solubility of intermediate lithium polysulfides (Li_2S_n, $4 \leq n \leq 8$) triggering the shuttle effect;[6] (ii) sluggish nucleation of the insulating discharge product Li_2S, limiting complete discharge;[7] and (iii) inherently poor sulfur conductivity impeding reaction kinetics.[8–10] These interconnected bottlenecks collectively constrain Li–S battery performance.

In this landscape, single-atom catalysts (SACs) characterized by atomically dispersed active sites, tunable coordination

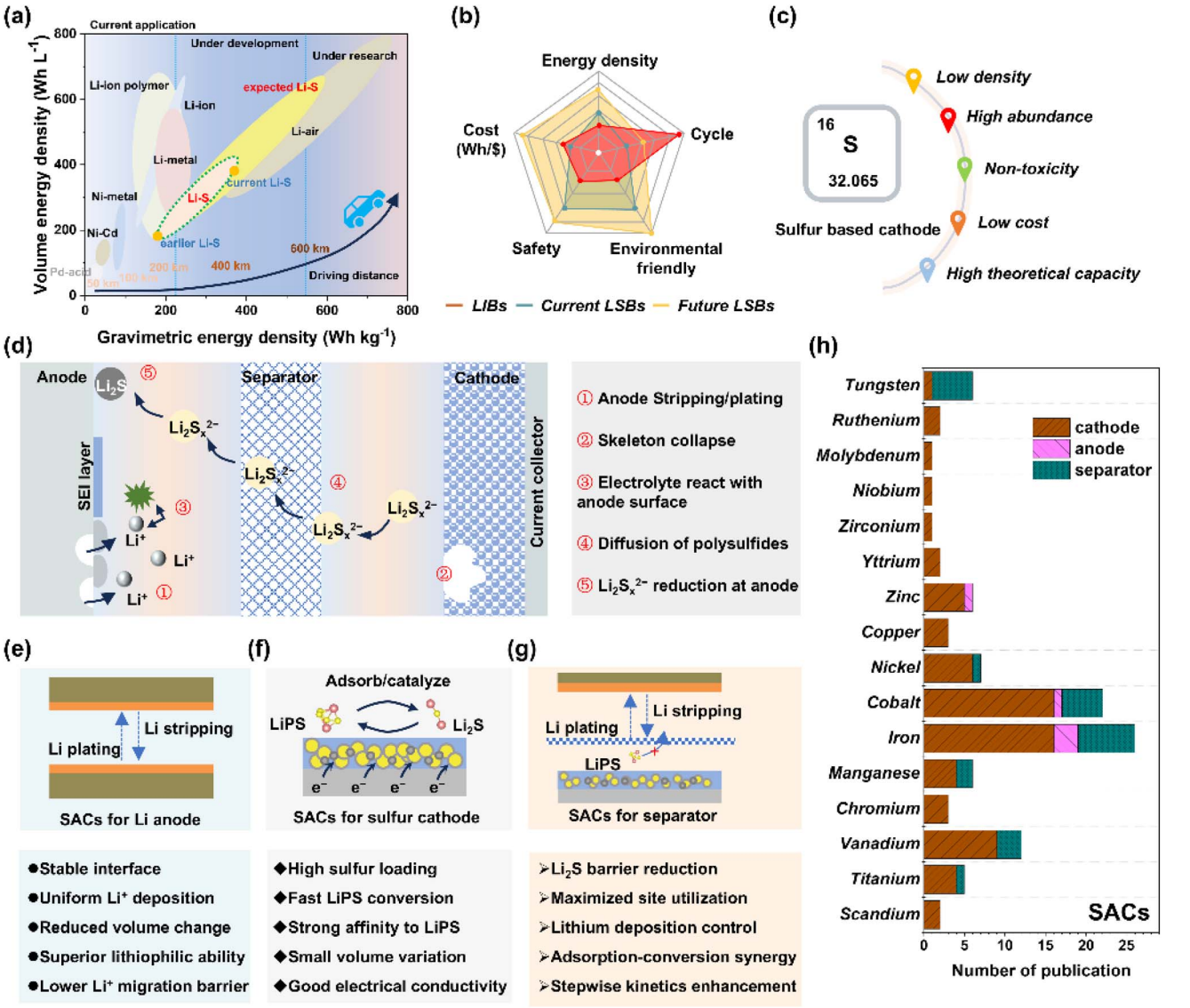

Fig. 1 Landscape of Li–S batteries and the emerging role of SACs. (a) Gravimetric and volumetric energy density comparison between Li–S batteries and state-of-the-art battery systems. Redrawn based on ref. 4. (b) Key advantages of Li–S batteries over lithium-ion batteries, including high theoretical energy density, low cost, and environmental compatibility. (c) Intrinsic merits of sulfur cathodes: high specific capacity, natural abundance, and low toxicity. (d) Major performance challenges in Li–S batteries: polysulfide shuttling, poor conductivity, and volume change. (e–g) Reported SAC modification strategies for (e) lithium metal anodes, (f) sulfur cathodes, and (g) separators, addressing interfacial and catalytic issues. (h) Distribution of SAC systems in Li–S batteries by functional location (anode, cathode, separator) and metal center, reflecting research focus and design diversity.

environments, and unique electronic structures have emerged as transformative mediators.[11–14] Current evidence confirms SACs not only anchor polysulfides and catalyze their conversion but also possess underutilized potential to redirect electrochemical pathways (the advantages of Li–S batteries and current progress are summarized in Fig. 1).[15–18] However, prevailing research remains fragmented, focusing on localized catalytic enhancements while lacking a unified theoretical framework to fully exploit SACs' capacity for reconstructing Li–S reaction mechanisms.[19]

To bridge the fragmentation gap between catalyst function and reaction mechanisms in Li–S batteries, we propose "precision catalysis" as a transformative paradigm for the deployment of SACs. This framework transcends conventional catalyst design by establishing a multidimensional, closed-loop control system characterized by predictability, schedulability, and feedback capability across the entire electrochemical landscape, including reaction pathways, interfacial dynamics, and structural evolution. Crucially, this shifts the role of SACs from passive adsorption–conversion promoters to active, programmable mediators of redox chemistry. Validation begins with a systematic deconstruction of the Li–S reaction cascade, specifically the challenges of polysulfide shuttling, interfacial conversion barriers, and Li_2S nucleation–deposition dynamics to identify the critical intervention nodes for SACs.

Guided by insights from SAC-related catalysis, we define a three-dimensional synergistic framework: spatial configuration engineering enables site-specific intermediate interaction *via* atomic site distribution, host–guest confinement, and electronic coupling;[20–22] reaction pathway engineering modulates redox trajectories by lowering energy barriers, stabilizing intermediates, and suppressing polysulfide shuttling;[23,24] and functional coupling provides dynamic control of electronic structure, solid-electrolyte interphase (SEI) tuning, and dual-site synergism through integration into responsive host frameworks.[25–27] Subsequently, this theoretical framework informs concrete material design strategies, including coordination microenvironment engineering, confinement-driven host architecture construction, and device-level hierarchical integration. Finally, the universality of precision catalysis is demonstrated by its successful extension to chemically analogous and structurally divergent systems, including sodium–

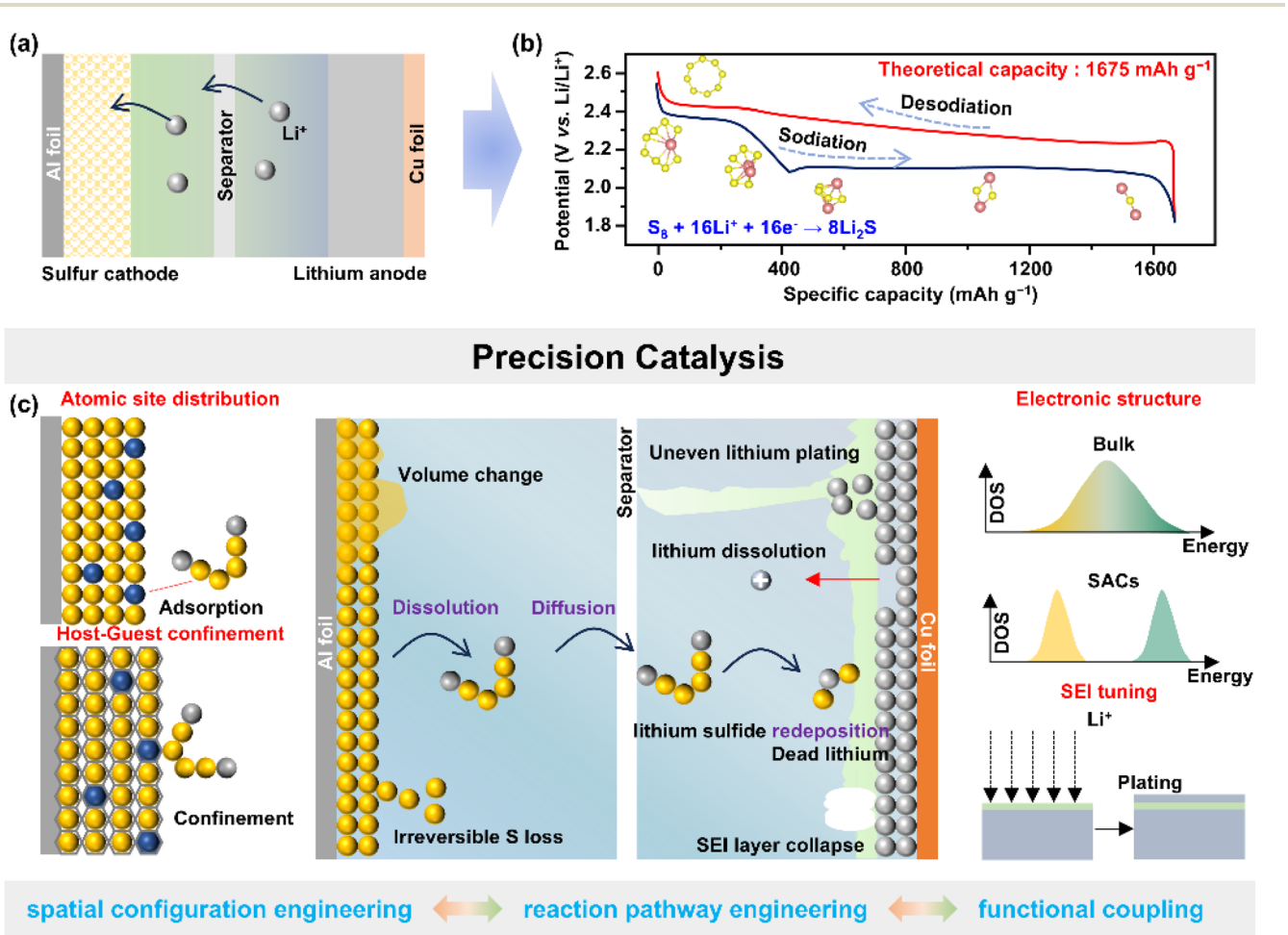

Fig. 2 Reaction mechanism and catalytic modulation in Li–S batteries. (a) Working principle of Li–S batteries, illustrating redox processes at the sulfur cathode and lithium metal anode. (b) Charge–discharge profiles with corresponding intermediate species (*e.g.*, Li_2S_8, Li_2S_6, Li_2S_4, Li_2S_2, Li_2S), elucidating the origin of high theoretical energy density. (c) Summary of recent SAC research in Li–S batteries and the proposed precision catalytic regulation strategy for spatial, electronic, and chemical modulation of redox pathways.

sulfur (Na–S), potassium–sulfur (K–S), Magnesium–sulfur (Mg–S), and solid-state Li–S batteries, showcasing broad applicability across multi-electron energy storage platforms.

The core contribution of this work resides in establishing a closed-loop correlation among catalytic behavior, reaction mechanisms, and material design. By recasting SACs as reaction-programming platforms rather than performance-enhancing additives, this framework lays the foundation for predictive, system-level electrochemical regulation. We anticipate that this precision-centered approach, integrating spatial configuration, reaction pathway control, and multi-field functional coupling, will catalyze paradigm-shifting advances in Li–S chemistry and beyond.

2. Mechanistic insights and precision catalysis theory: SACs as reaction architects

The exceptional energy density of Li–S batteries, rooted in the multi-electron conversion of cyclo-S_8 to crystalline Li_2S,[11,28,29] is intrinsically challenged by its stepwise reaction pathway (as illustrated in Fig. 2a and b). Unlike intercalation cathodes, sulfur reduction proceeds through a sequence of soluble polysulfide intermediates from S_8 to Li_2S_6, then Li_2S_4, Li_2S_2, and finally Li_2S. This multi-step process induces complex interfacial dynamics involving dissolution, diffusion, and re-deposition, all electrochemically coupled with Li_2S nucleation barriers.[6,30,31] This "solid–liquid–solid" progression establishes critical interdependencies between interfacial chemistry, reaction trajectory, and electrode architecture. SACs, with their atomically dispersed active sites, tunable coordination environments, and unique electronic structures, have emerged as transformative mediators capable of fundamentally reconfiguring this electrochemistry. This chapter first elucidates the multifaceted mechanistic roles of SACs in addressing the core Li–S bottlenecks, establishing their capability as more than just catalysts. Building upon this foundation, we then introduce the *precision catalysis theory*, a three-dimensional control paradigm encompassing spatial configuration engineering, reaction pathway engineering, and functional coupling (as shown in Fig. 2c). This framework transitions SACs from localized accelerators to systemic architects capable of predictively scheduling Li–S reactions.

2.1 Addressing core Li–S bottlenecks: multifunctional roles of SACs

SACs fundamentally reconfigure Li–S electrochemistry through dual yet synergistic functions:[32–34] Chemical confinement *via* lithiophilic/sulfiphilic sites (*e.g.*, M–N–C moieties) immobilizes soluble lithium polysulfides (LiPSs) within cathodic domains, suppressing shuttle-driven capacity fade.[35–37] Exemplified by $Co–N_4$ centers, strong chemisorption through Li–N/O or M–S bonding depletes electrolyte LiPS concentrations,[15,38,39] while concurrently, these atomic sites catalyze bidirectional sulfur redox, lowering activation barriers for both Li_2S deposition and its oxidative decomposition. Carbon nanotube-encapsulated Co SACs epitomize this duality, enhancing kinetics while curtailing active material loss.[40] Critically, shuttle suppression originates not merely from adsorption but through SAC-enabled cascade catalysis: d-orbital-rich metal centers (*e.g.* Fe, Co, Mn) immobilize LiPSs *via* Lewis acid–base interactions while stabilizing transition states to accelerate their complete conversion. π-Conjugation-engineered electron-deficient $Co–N_4$ sites intensify such effects (Fig. 3a and b).[41]

Beyond this foundational adsorption–conversion synergy, SACs induce deeper mechanistic shifts. *Operando* analyses demonstrate that SACs shift the sulfur reduction mechanism from a sequential process involving conversion of long-chain LiPSs to short-chain LiPSs and finally Li_2S to parallel pathways enabling concurrent consumption of both long- and short-chain intermediates.[42,43] Co SACs drive this toward zero-order kinetics, minimizing transient LiPS accumulation.[42] Concomitantly, SACs dictate Li_2S nucleation and deposition behavior: metal–Li_2S bond strength governs deposition efficacy, with strong-binding sites ($V–N_4$, Co–N/C, and Fe–N/C) dramatically reducing dissociation energies to enable uniform electrodeposition, contrasting sharply with ineffective weak-binders (*e.g.*, Cu–N/C, Ag–N/C).[44,45] Vanadium SACs ($V–N_4$@graphene), exhibiting minimal Li_2S decomposition barriers (Fig. 3c–f),[44] exemplify how catalytic Li_2S re-oxidation prevents electrochemically inactive sulfide accumulation and sustains active material recycling. Kinetic bottlenecks are similarly dismantled, asymmetric $Fe–N_3C_2$ coordination facilitates S_8 ring-opening *via* σ–π intermediate stabilization, while $Fe–N_3C_2–C/Li_2S_6$ interfacial motifs leverage boundary effects to direct Li_2S nucleation (Fig. 3g–i).[46] Ultimately, SACs resolve Li_2S deposition mismatches by templating growth at high-energy surfaces. Molybdenum assembling heterostructures exemplify this, elevating Li_2S deposition plateaus through interfacial bias to circumvent pore clogging and dead zone formation. Further extending functionality, SAC lithiophilicity guides homogeneous Li plating, indirectly stabilizing anode interfaces.[47–49]

Collectively, SACs transcend conventional catalyst paradigms, evolving from electron-transfer facilitators to reaction architects. Their tripartite functionality, adsorptive anchoring for LiPS confinement, interfacial modulation for barrier depression, and programmed guidance for phase-selective deposition, engineers controllable reaction coordinates. This mechanistic framework provides the essential foundation for predictive design, where quantitative descriptors correlating SAC configuration with Li_2S redox kinetics crystallize into blueprints for rational catalyst development (Fig. 3j–m).[50] It is precisely this capacity for multi-faceted intervention that enables the shift towards a paradigm of *precision regulation via spatial configuration engineering, reaction pathway engineering, and functional coupling*.

2.2 The precision catalysis paradigm in three dimensions

Conventional Li–S catalysts remain confined by unidirectional "strong adsorption–weak conversion" limitations, unable to synergistically balance polysulfide anchoring, multi-step kinetics, and interfacial evolution (Fig. 4a and b).[24,51–54] The

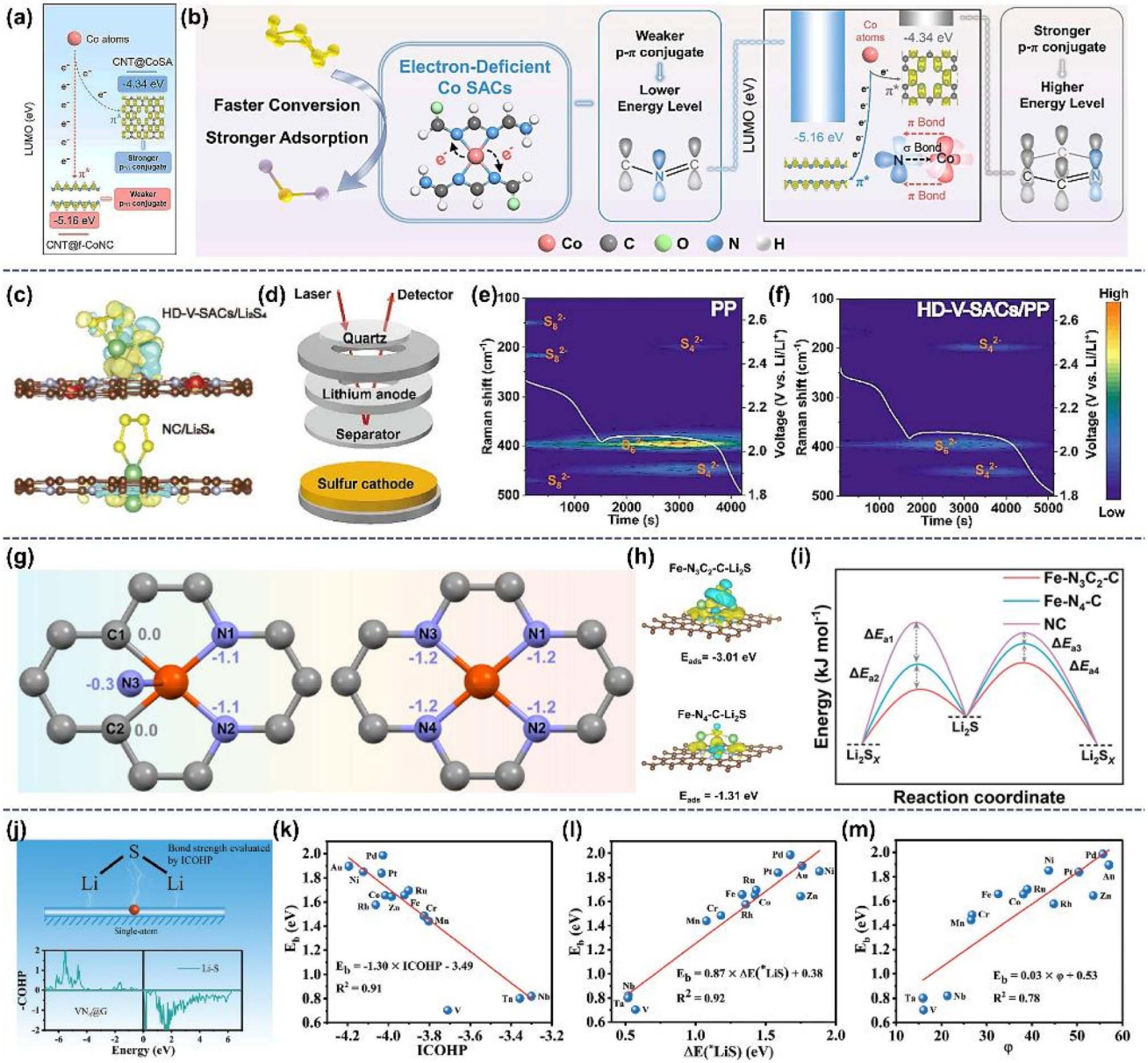

Fig. 3 Coordination environment and electronic structure effects on sulfur redox catalysis. (a) Lowest unoccupied molecular orbital (LUMO) energy levels and charge transfer diagrams of CNT@f-CoNC and CNT@CoSA. (b) Synthesis schemes of CNT@f-CoNC and CNT@CoSA with distinct Co single-atom coordination environments. Reproduced from ref. 41 with permission from Wiley-VCH GmbH, Copyright 2025. (c) Charge density difference of Li_2S_4 adsorption on HD-V-SACs and NC. (d) *In situ* Raman setup for monitoring Li–S reactions. Time-resolved Raman spectra for batteries with (e) a pristine polypropylene (PP) separator and (f) HD-V-SAC-modified PP separator. Reproduced from ref. 44 with permission from the Royal Society of Chemistry, Copyright 2025. (g) Bader charge analysis of Fe–N_3C_2–C and Fe–N_4–C configurations. (h) Charge density difference for Li_2S on Fe–N_3C_2–C and Fe–N_4–C. (i) Calculated activation energies for Li_2S precipitation and decomposition on different Fe–N_x sites. Reproduced from ref. 46 with permission from the American Chemical Society, Copyright 2022. (j) Decomposition mechanism of Li_2S and crystal orbital Hamilton population (COHP) analysis on VN_4@graphene (VN_4@G). Correlation plots of Li–S interaction energy (E_b) *versus* integrated COHP values (k, ICOHP), reaction intermediate binding energy ΔE (l, *LiS), and work function (m, ϕ), with fitted liner trends and R^2 values. Reproduced from ref. 50 with permission from Wiley-VCH GmbH, Copyright 2021.

atomically precise coordination, tunable electronic structures, and near-unity atom utilization of SACs empower them to redefine this landscape. Building upon their proven mechanistic capabilities (Section 2.1), SACs achieve a paradigm shift, moving beyond adsorption-centric approaches towards active reaction scheduling. This *precision catalysis theory* integrates three synergistic dimensions of spatial configuration engineering, reaction pathway engineering, and functional coupling to reimagine catalytic intervention in Li–S systems.

2.2.1 Spatial configuration: asymmetry design and confinement effects. Spatial configuration engineering manifests through engineered atomic asymmetry, atomic site distribution, host–guest confinement, and electronic coupling. Breaking symmetric coordination constraints, as realized in Fe–

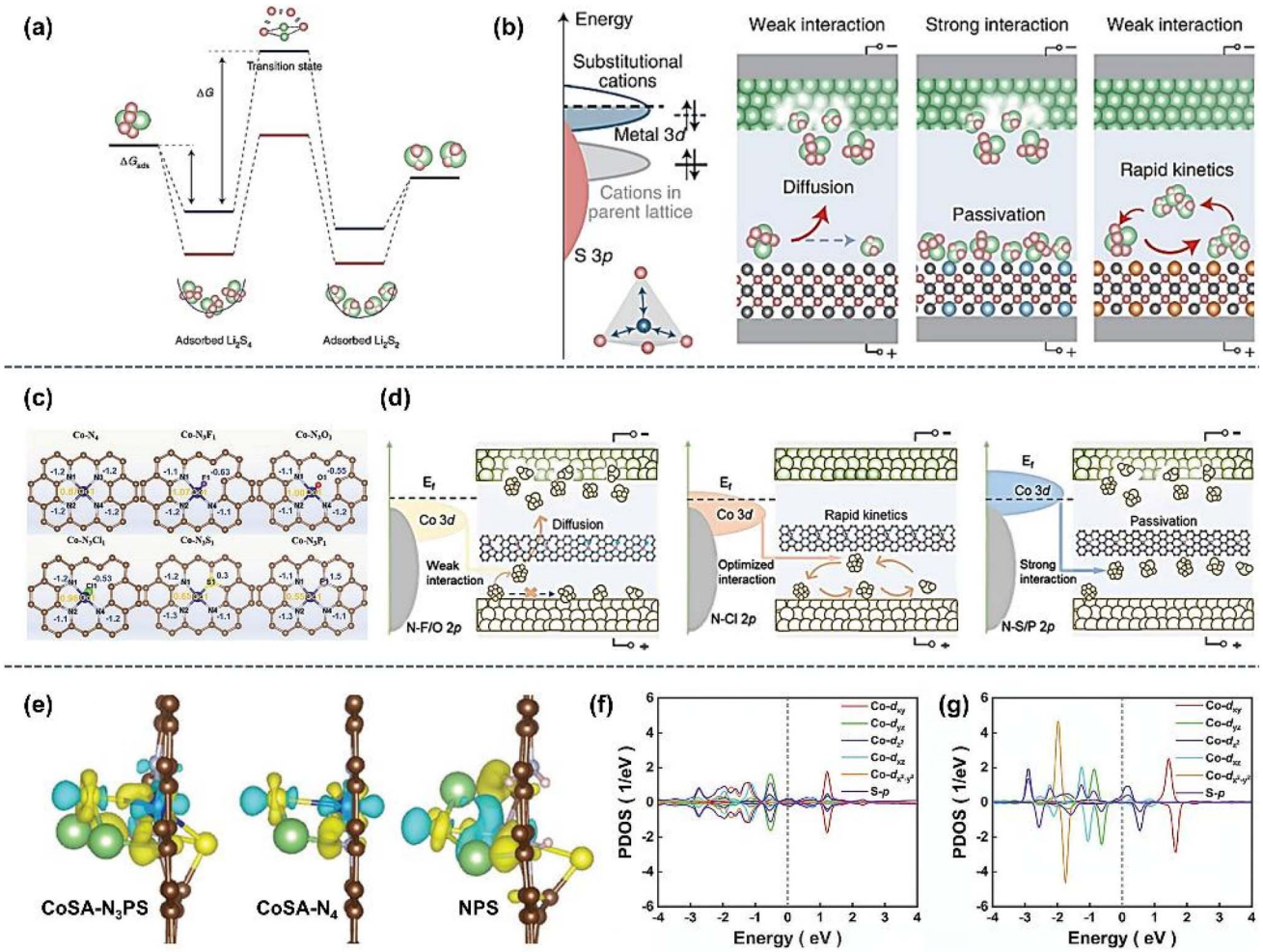

Fig. 4 Coordination engineering and electronic coupling toward enhanced LiPS conversion. (a) Simplified energy diagram of the liquid–solid conversion from Li_2S_4 to Li_2S_2. (b) Conceptual illustration of weak, moderate, and strong interactions between polysulfides and catalytic centers. Reproduced from ref. 51 with permission from Springer Nature Limited, Copyright 2022. (c) Bader charge transfer values of Co–N_4 and Co–N_3X_1 configurations. (d) Schematic of catalytic differences induced by asymmetric Co–N_3X_1 coordination environments. Reproduced from ref. 55 with permission from Wiley-VCH GmbH, Copyright 2024. (e) Simulated charge density difference for Li_2S adsorption on CoSA–N_3PS, CoSA–N_4, and NPS configurations. PDOS of Co-d orbitals and S-p orbitals in Li_2S on (f) CoSA–N_3PS and (g) CoSA–N_4. Reproduced from ref. 56 with permission from Wiley-VCH GmbH, Copyright 2024.

N_3C_2 or mixed M–N/O sites, induces localized charge polarization that selectively enhances adsorption of pivotal intermediates like Li_2S_4.[46] This phenomenon, interfacial polarization, is amplified by host architectures. Porous carbon cavities and graphene defect edges not only anchor metal atoms *via* high migration barriers but also establish integrated microzones that enable continuous adsorption, fixation, and conversion processes. SAC-derived Co-coordination asymmetric configurations (*e.g.*, CoSA–N_3PS, Co–N_3Cl_1) exemplify this dual advantage, delivering unparalleled Li_2S_4 affinity and cleavage kinetics through open coordination geometries unattainable in conventional symmetric sites (Fig. 4c and d).[55–57] The projected density of states (PDOS) analysis shows that Li_2S on the CoSA–N_3PS substrate exhibits stronger d–p orbital hybridization at the Fermi level compared to CoSA–N_4, while the absence of Co–S hybridization in the density of states (DOS) of CoSA–N_3PS indicates that P and S coordination effectively tunes the electronic structure of the Co center and enhances its interaction with S through d–p orbital overlap (Fig. 4e–g).

In essence, modifying the coordination environment of a single atom directly influences how LiPSs bind and react. For instance, an open Co–N_3PS site can polarize the electron density to strengthen Li_2S_4 adsorption and accelerate its reduction, whereas a symmetric Co–N_4 site lacks the same tunability. This direct structure–function correlation exemplifies the spatial precision of SACs, as seen in the CoSA–N_3PS *versus* CoSA–N_4 comparison.

2.2.2 Reaction pathway control: adaptive kinetic programming. Reaction pathway engineering unfolds through adaptive process control like adjusting the energy barriers, intermediates, and polysulfide shuttling, where SACs dynamically modulate reaction routes to overcome kinetic bottlenecks in real time. Crucially, this adaptability stems from SACs actively participating in and directing key electrochemical steps. For

instance, addressing the critical and often sluggish reduction of soluble intermediates (*e.g.*, S_4^{2-}) to the final solid discharge product Li_2S, specific SAC configurations play distinct catalytic roles. Ni-based sites demonstrably guide Li_2S nucleation through the formation of reversible Ni–S_x intermediates, effectively lowering the energy barrier for this crucial phase transition. During Li_2S_4 adsorption, the Fe–N_4 center exhibits higher electron density near the Fermi level compared to the Ni–N_4 center, reflecting better conductivity and stronger LiPS capture capability, which in turn contributes to enhanced catalytic activity for both liquid–liquid and liquid–solid conversion processes (Fig. 5a and b).[58] Concurrently or alternatively, through cooperative electronic structure engineering, such as sulfur substitution in Co–N_4 coordination environments or electron-exchangeable binding (EEB) site-induced modulation of the d-band center in Fe–N–C frameworks, single-atom catalysts achieve enhanced d–p orbital hybridization or controlled electron transfer. This enables stronger LiPS anchoring and directly facilitates Li_2S conversion, thereby circumventing the sluggish multistep kinetics typical of conventional Li–S cathodes (Fig. 5c and d).[59,60]

Similarly, during the oxidation (charge) process, which faces significant kinetic challenges in decomposing Li_2S/Li_2S_2, SACs exert tailored control. Mn centers, leveraging their charge-delocalized electronic states, effectively weaken Li–S bonds, facilitating their decomposition back to soluble polysulfides.[61] Complementing this mechanism, Co sites establish highly efficient electron-transfer loops *via* valence cycling between Co^{2+} and Co^{3+} states, accelerating the overall oxidation kinetics.[62,63]

Strong evidence supporting this concept of SACs as active participants comes from *operando* characterization techniques, which show them functioning as "reaction co-evolvers". Specifically, studies demonstrate that Co–N_4 sites dynamically form transient Co–S bonds during the discharge process, directly engaging with sulfur species, before regenerating their original coordination upon charge completion (Fig. 5e).[64] This phenomenon of adaptive bonding is pivotal, as it allows SACs to

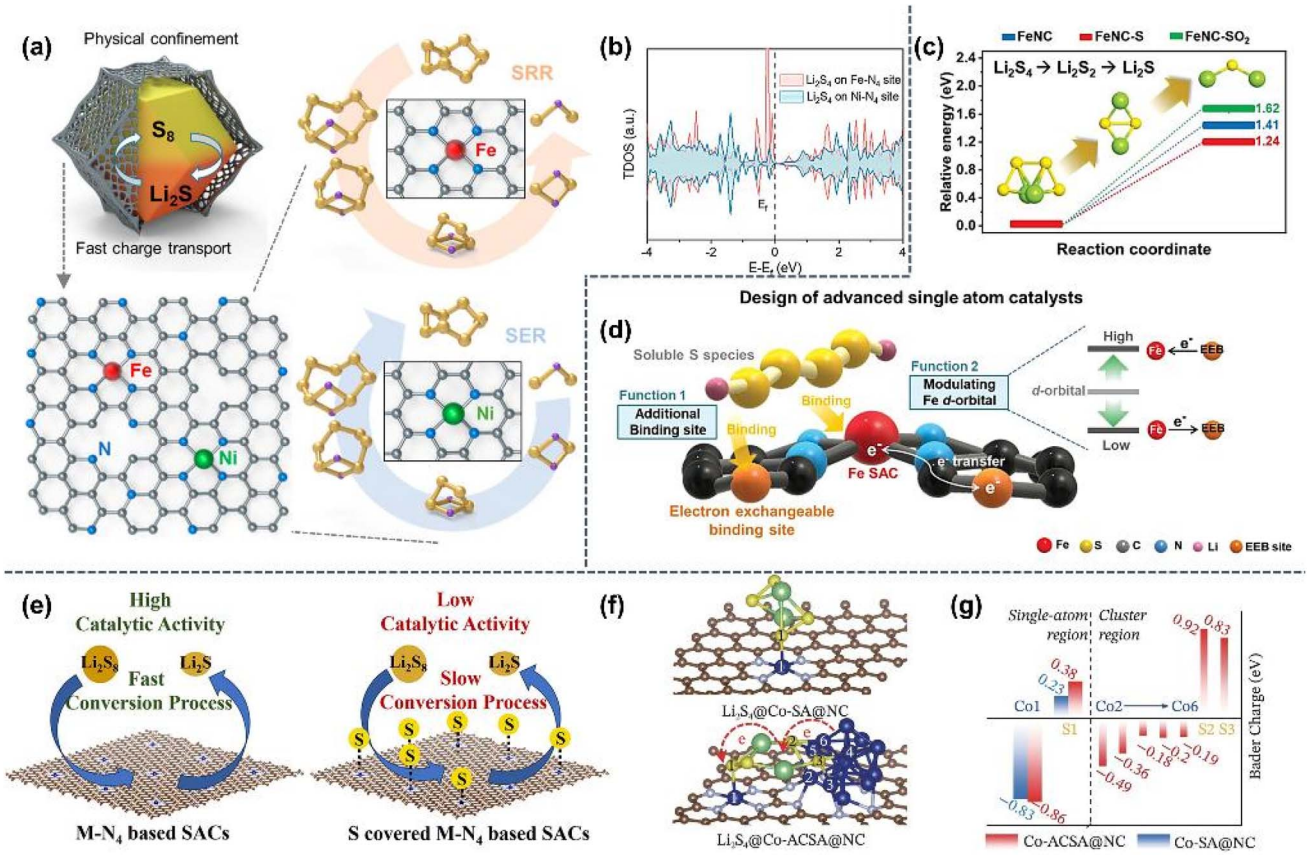

Fig. 5 Bidirectional catalysis and coordination asymmetry in polysulfide conversion. (a) Schematic of bidirectional catalytic behavior of Ni–Fe–NC for accelerating both polysulfide reduction and Li_2S oxidation. (b) Total density of states (TDOS) analysis of Ni–N_4 and Fe–N_4 sites with Li_2S_4 adsorption. Reproduced from ref. 58 with permission from the American Chemical Society, Copyright 2023. (c) Calculated reaction energy barriers for Li_2S_4 to Li_2S conversion on FeNC, FeNC–S, and FeNC–SO_2 catalysts. (d) Schematic of EEB sites near Fe–N–C: (function 1) forming bonds with LiPSs; (function 2) modulating the Fe d-orbital *via* electron exchange. Reproduced from ref. 59 with permission from Wiley-VCH GmbH, Copyright 2023. (e) Atomic schematic of the sulfur poisoning effect in SACs. Reproduced from ref. 64 with permission from the American Chemical Society, Copyright 2023. (f) Models of Li_2S_4 adsorbed on CoACSA@NC and Co-SA@NC with asymmetric coordination. (g) Bader charge analysis comparing charge distribution in CoACSA@NC and Co-SA@NC systems. Reproduced from ref. 66 with permission from Wiley-VCH GmbH, Copyright 2025.

balance catalytic efficiency with facile product release. Consequently, sulfur poisoning of active sites is mitigated while maintaining high catalytic turnover, provided the M–S bond strength is optimized within a specific energetic window.[65–67] Surrounded by the highly electronegative N atoms, the Co atom in the Co–N_4 moiety delivers a relatively electron-deficient state that readily coordinates with the electron-rich S in polysulfides. As for the nanocluster, Co atoms in the main body are relatively metallic, with abundant delocalized electrons to be readily donated to the amphiphilic LiPSs, resulting in the establishment of Co–S bonding. More interestingly, such an electron transfer further strengthens the Co–S interaction at the CoN_4 moiety, as confirmed by Bader charge analysis (Fig. 5f and g).[66] Therefore, reaction pathway engineering fundamentally ensures the sulfur redox reactions dynamically follow the most kinetically favorable pathway dictated by the SAC's unique electronic and coordination structure at each stage of the electrochemical cycle.

Another critical mechanistic consideration is catalyst pre-sulfurization. Certain catalysts are designed to transform into their active sulfide phase *in situ* during cycling. For example, Co_4N can convert to CoS_x upon exposure to polysulfides, dynamically generating active sites. While this transformation may delay initial activity, it offers ongoing regeneration of catalytic interfaces. In contrast, pre-sulfurized catalysts offer immediate LiPS affinity but may accumulate insulating Li_2S/Li_2S_2 species over time, passivating active sites. Thus, there is a trade-off: pre-sulfurized catalysts enable rapid activation but risk surface passivation, whereas unsulfurized catalysts require activation yet yield more resilient interfaces post transformation.[68,69]

Beyond these mechanistic specifics, it is informative to contrast single-atom catalysts with small cluster catalysts, as their catalytic behaviors can diverge significantly. A multi-atom cluster provides multiple adjacent metal centers that can interact cooperatively with intermediates (for example, a Li_2S_n species might bridge between two metal atoms), potentially lowering certain reaction barriers *via* ensemble effects. In contrast, a SAC features isolated metal atoms that operate independently, ensuring a uniform active site environment but precluding such multi-site interactions. Mechanistically, clusters may offer alternative adsorption or activation modes (*e.g.*, dual-site binding of a single intermediate) that are unavailable to a single atomic site, possibly enhancing reaction thermodynamics or kinetics in specific steps. SACs, however, compensate through precisely tunable coordination environments for each site, and adjustments in local geometry or electronic structure can modulate binding strengths to target rate-limiting steps with high selectivity. Structurally, the active site of a SAC is an atom dispersed on a support (anchored by coordination to surface heteroatoms), whereas cluster catalysts consist of a few metal atoms bonded together. This means every metal atom in a SAC is exposed and catalytically active (maximizing atom utilization), while clusters contain interior atoms that contribute less to surface reactivity. From a stability perspective, isolated single atoms can be strongly stabilized by the support (through covalent bonds or coordination), often making them resistant to aggregation under operating conditions. Clusters, by contrast, may undergo coalescence into larger particles over long cycles if not well confined, though their initial metal–metal bonds can confer short-term stability against dissolution. Moreover, SACs offer unparalleled tunability: because all sites are equivalent and well-defined, one can systematically alter the ligand environment or electronic state of the active center (*via* support or dopant engineering) to optimize performance, an experimental and theoretical advantage in establishing clear structure–activity relationships. In summary, while metal clusters can in some cases provide multisite synergistic effects that improve certain catalytic metrics, SACs distinguish themselves through single-site precision, highly controllable reactivity, and nearly 100% active atom utilization. These attributes underscore the SAC's role in the precision catalysis paradigm, where uniformity and programmability of active sites are leveraged to achieve closed-loop, targeted reaction control.[70–72]

2.2.3 Functional coupling: multiphysics responsiveness and diagnostic integration. Functional coupling significantly extends the capabilities of SACs beyond intrinsic electrochemistry by integrating multi-field responsiveness with diagnostic intelligence (*e.g.*, digital twin, some of the concepts in this chapter are derived from interdisciplinary fields and may not have been applied in this field yet), enabling adaptive regulation under complex conditions like dynamic control of electronic structure, SEI tuning, and dual-site synergism through integration into responsive host frameworks. Drawing inspiration from mechanics, a compelling example exploits mechanical stress generated by substantial volume changes (larger than 80%) during Li_2S deposition,[73] where certain SACs harness d-orbital splitting to activate strain-responsive catalytic pathways under compression.[74–78] Concurrently, principles adapted from polymer science inform the use of elastic hosts that maintain electrode contact integrity despite severe volume fluctuations, preserving electrochemical activity under strain.[79]

Strategically applying concepts from photonics and electromagnetics, external fields provide precise non-electrochemical control levers to enhance SAC activity and modulate kinetics. For example, light excitation on heterostructures like In_2S_3/Ti_3C_2 boosts the activity of embedded Pt SACs for polysulfide conversion, simultaneously promoting more homogeneous Li^+ deposition patterns at the anode.[80] Similarly, magnetic fields can be utilized to optimize electron transfer kinetics of nitrates to ammonia by manipulating spin states within SACs.[81] Additionally, directional electric fields can stabilize critical transition states,[82–84] lowering the activation barrier for challenging steps such as Li_2S_6 cleavage, offering a means to fine-tune reaction energetics.

Critically, these multi-field controls converge seamlessly with advanced *in situ* diagnostics inspired by materials characterization (*e.g.*, XANES for chemical state analysis, environmental TEM for real-time morphological evolution).[85] This integration forms responsive "catalyst-battery" networks capable of providing real-time feedback on the state of the catalyst and the ongoing reactions, enabling reactivity modes beyond conventional electrochemistry. Such closed-loop intelligence, conceptually borrowed from cybernetic systems,

pioneers applications like photo-activated energy converters and self-adjusting battery systems that modulate operational parameters (*e.g.*, charge rates or field intensity) based on catalyst/reaction feedback.[86–88] This embodies the essence of functional coupling.

This three-dimensional synergy of spatial configuration engineering, reaction pathway engineering, and functional coupling elevates SACs from localized accelerators to systemic architects. Spatially engineered sites establish adsorption selectivity; adaptive processes overcome kinetic bottlenecks; field-responsive systems introduce operational intelligence. The paradigm addresses persistent Li–S challenges while demonstrating adaptability for extension to Na–S, K–S, and Mg–S systems and solid-state configurations. Quantitative descriptors correlating SAC structure with Li_2S redox kinetics, emerging from mechanistic studies, crystallize this approach into a predictive framework,[50] positioning SACs as programmable directors of multi-electron energy storage. The subsequent chapter will translate this precision catalysis theory into concrete material construction strategies.

2.3 Distinction from conventional catalytic paradigms

Conventional catalyst design in rechargeable batteries has traditionally relied on one-dimensional strategies targeting specific limiting steps. For example, in Li–S systems, carbonaceous hosts or polar additives are introduced to adsorb polysulfides and thereby mitigate the polysulfide shuttle effect, while catalytic nanoparticles are employed to accelerate Li_2S nucleation during discharge. Similarly, in Li–O_2 and Zn–air batteries, catalytic paradigms are often constructed around volcano-plot relationships derived from single activity descriptors such as oxygen binding energy for the ORR/OER.[89–92] These approaches emphasize open-loop, single-site optimization, where catalysts are tuned to improve an isolated reaction step without dynamically responding to the evolving multi-phase electrochemical environment.

By contrast, the precision catalysis paradigm proposed in this review represents a multi-dimensional, closed-loop strategy. Rather than passively lowering energy barriers or simply anchoring intermediates, precision catalysis leverages SACs to program the entire reaction trajectory through three synergistic axes: (i) spatial configuration engineering, which defines site-specific interactions *via* tailored coordination asymmetry and host–guest confinement; (ii) reaction pathway engineering, which actively guides intermediate stability and transition-state energetics to reshape conversion sequences; and (iii) functional coupling, which enables dynamic feedback through electronic, interfacial, or external-field interactions. Importantly, this paradigm allows predictive and adaptive control of redox chemistry, positioning catalysts as programmable regulators of reaction networks rather than static active sites.

Comparisons with other electrochemical systems underscore the novelty of this approach. For instance, in Li–O_2 batteries, SACs have been employed to optimize oxygen reduction and evolution *via* d-band tuning, yet these strategies remain constrained by Sabatier scaling and function primarily as linear optimizers.[93] Similarly, in Zn–air systems, Mn- and Co-based SACs have been introduced to lower ORR/OER barriers, but the emphasis is again placed on thermodynamic descriptors rather than dynamic feedback.[94,95] In Na–S batteries, conventional electrocatalysts attempt to stabilize sodium polysulfides but lack the spatial and functional programmability needed to simultaneously suppress solubility and accelerate kinetics.[96] In all of these cases, the absence of multi-field coordination and closed-loop adaptability limits catalyst performance to incremental improvements. Precision catalysis, by integrating spatial, kinetic, and functional dimensions, transcends these conventional paradigms and provides a systematic route to reconstruct electrochemical logic rather than merely alleviating bottlenecks.

Despite its promise, precision catalysis is not without challenges. Its inherent complexity demands sophisticated synthetic strategies to stabilize well-defined atomic environments, advanced *in situ* characterization to capture dynamic feedback, and multi-scale modeling to correlate atomic events with cell-level performance. Scaling up is particularly difficult, as reproducing atomically dispersed, feedback-responsive architectures in bulk quantities remains non-trivial. These challenges highlight the need for continued innovation in both experimental and theoretical methodologies to fully realize the potential of precision catalysis.

3. Materials design strategies: from theory to structural realization

Building upon the "spatial configuration engineering, reaction pathway engineering, and functional coupling" established in Chapter 2, this chapter outlines the material realization pathways. Our strategy adopts a multi-scale progressive approach: commencing at the atomic scale for active site engineering, extending to micro/nano-scale host architecture design, and culminating in device-level integration, thereby systematically translating theoretical control principles into tangible structures.

3.1 Atomic-scale engineering: coordination design for spatial and kinetic control

The construction of SAC active centers fundamentally relies on robust coordination anchoring strategies and is central to spatial configuration engineering. Prototypical symmetric M–N_4 sites (*e.g.*, Fe–N_4, Co–N_4) effectively suppress polysulfide shuttling and enhance sulfur redox kinetics by tuning d-orbital electronic structures to lower S–S bond cleavage barriers.[32–37,40] However, symmetric M–N_4 coordination may bind LiPS intermediates too weakly or too strongly in a fixed manner and often fails to optimally stabilize all polysulfide species. Crucially, the principle of spatial precision is advanced by engineering coordination asymmetry to address these limitations. Introducing hetero-coordination environments (*e.g.*, M–N_3C_1, M–N_3S, M–N/O) disrupts local symmetry, inducing charge polarization, internal electric field gradients, and uneven electron density

around the metal center. This asymmetry underpins reaction pathway engineering, enabling directional adsorption of key LiPS intermediates and steering selective conversion pathways. For instance, replacing one N with C in M–N_3 (forming M–N_2C_1) induces asymmetrical electron density and lowers energy barriers for LiPS conversion. Increasing nitrogen coordination in Mo–N_xC_{3-x} SACs enhances polysulfide adsorption energy due to nitrogen's higher electronegativity. Mo–N_1C_2's low d-band center (−1.02 eV) causes insufficient adsorption, exacerbating shuttle effects, while Mo–N_2C_1's moderate d-band center (−0.95 eV) enables optimal LiPS adsorption, facilitating efficient conversion and discharge product desorption. This design achieves high-loading performance: a 7.75 mg cm^{-2} sulfur cathode delivers 5.08 mA h cm^{-2} initial areal capacity, retaining 3.86 mA h cm^{-2} after 180 cycles (Fig. 6a–c).[97] While asymmetric Cu–N_1C_2 sites on MXene exhibit stronger binding and faster Li_2S_2/Li_2S formation kinetics compared to symmetric Cu–N_3, as the Cu single atoms anchored on N-doped $Ti_3C_2T_x$ display higher binding energies and denser electron cloud overlap with lithium polysulfides than pristine $Ti_3C_2T_x$, reflecting the enhanced interaction and catalytic capability of single Cu sites toward LiPS conversion (Fig. 6d and e).[98] Recent

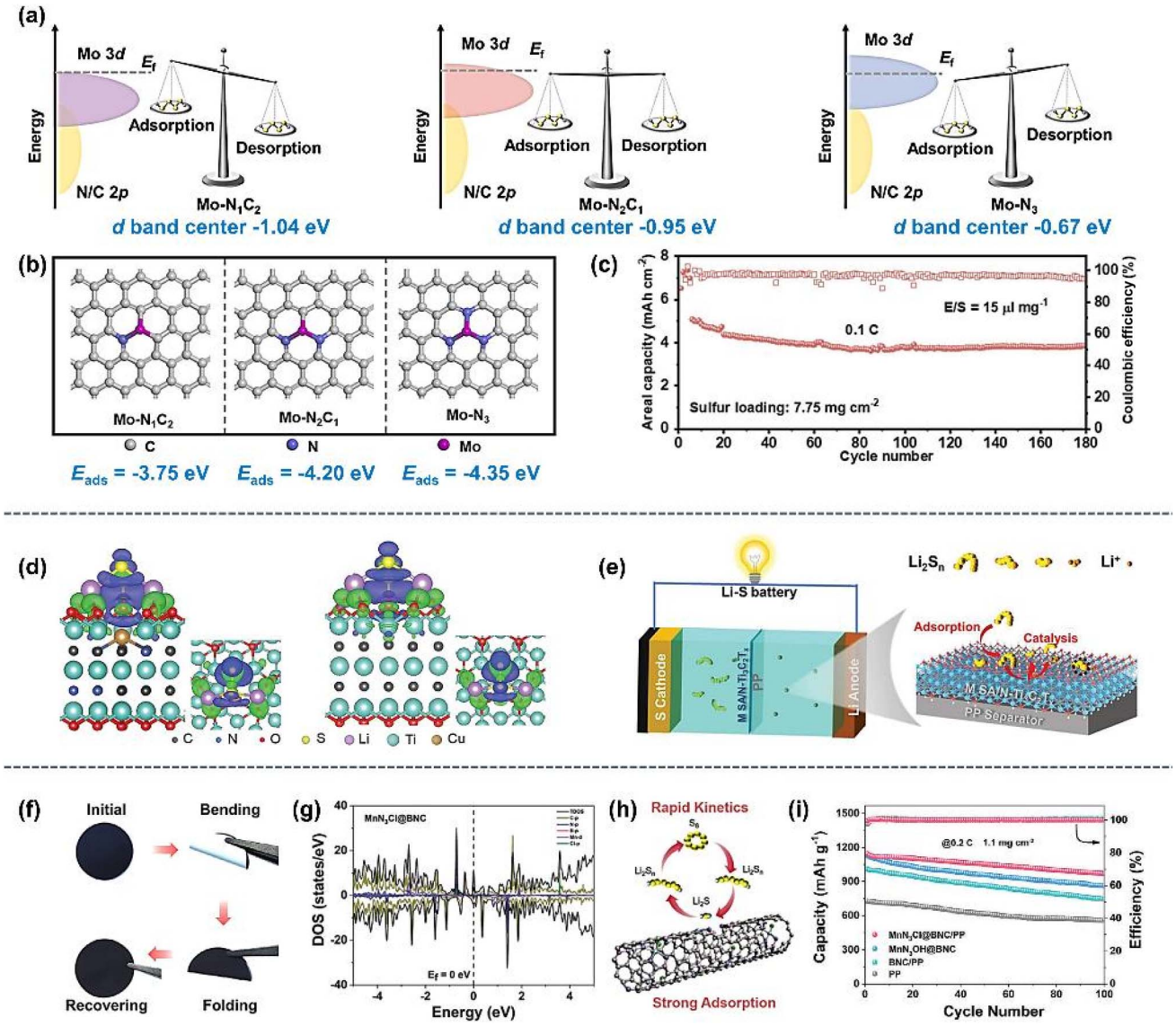

Fig. 6 Electronic descriptor-guided design of SACs for polysulfide regulation. (a) Sabatier-type trade-off correlation between the d-band-center position of catalyst active sites and LiPS adsorption–desorption capacity. (b) Optimized atomic structures of Mo–N_1C_2, Mo–N_2C_1, and Mo–N_3. (c) Cycling performance of the Mo–N_2C_1 catalyst at a sulfur loading of 7.75 mg cm^{-2} and 0.1C. Reproduced from ref. 97 with permission from Elsevier, Copyright 2023. (d) Differential charge-density of Li_2S_2 adsorption on Cu SA/N–$Ti_3C_2O_2$ and $Ti_3C_2O_2$. (e) Schematic of Li–S batteries with M SA/N–$Ti_3C_2T_x$-modified PP separators (M = Co, Ni, Mn, Zn, In, Sn, Pb, Bi). Reproduced from ref. 98 with permission from Wiley-VCH GmbH, Copyright 2023. (f) Digital photographs of modified separators showing flexibility. (g) DOS of MnN_3Cl@BNC. (h) Schematic of LiPS adsorption and conversion mechanism on MnN_3Cl@BNC. (i) Cycling performance of a MnN_3Cl@BNC-based Li–S battery at 0.2C. Reproduced from ref. 101 with permission from Wiley-VCH GmbH, Copyright 2024.

works vividly exemplify this principle: a Co SAC with Co–N_3S coordination exhibited significantly stronger polysulfide immobilization and faster conversion kinetics than symmetric Co–N_4, owing to the dual lithiophilic–sulfiphilic nature of its mixed N/S ligands.[99] Similarly, Fe–N_3S sites facilitate polysulfide adsorption/conversion more effectively than Fe–N_4 due to altered d-band centers.[100] A Mn SAC incorporating chlorine (Mn–N_3Cl) substantially lowered the critical Li_2S_2-to-Li_2S conversion barrier compared to Mn–N_4, highlighting how tailored ligand fields fine-tune catalytic pathways. Its higher electron density at the Fermi level and narrower band gap indicate enhanced conductivity, while the MnN_3Cl@BNC/PP composite achieves a stable capacity of 969 mA h g^{-1} with only 0.15% capacity decay per cycle over 100 cycles at 0.2C, confirming its superior electrochemical stability (Fig. 6f–i).[101] Furthermore, V–N_4@graphene SACs demonstrated minimal Li_2S decomposition barriers (1.24 eV), enabling complete re-oxidation.[44] These studies underscore that precisely tuning spatial coordination (*e.g.*, M–N_4 *vs.* M–N_3C_1 *vs.* M–N_2O_2) optimizes binding energies across sulfur species, balancing polysulfide adsorption and catalytic conversion. A rich variety of asymmetric environments, including N/O dual-coordination and diatomic pair sites, is now being explored to maximize catalytic selectivity in Li–S chemistry.[100]

3.2 Micro/nanoscale hosts: confined architectures for enhanced coupling

Transitioning to the micro/nano-scale, the design of host matrices (*e.g.*, hollow structures, hierarchical porosity, interlayers, and 3D frameworks) is paramount as it directly governs electrolyte penetration, intermediate diffusion dynamics, Li^+ transport, and critically, Li_2S nucleation and deposition behavior. These factors are central to achieving effective spatial configuration engineering (confinement) and enabling reaction pathway programming. Hierarchical porous architectures, particularly hollow structures, synergize powerfully with SACs to create confined catalytic nanoreactors. Hollow carbon shells, exemplified by those derived from ZIF-8 MOFs, physically restrict polysulfide diffusion outwards while their conductive surfaces facilitate electron transfer and guide more uniform Li_2S deposition, significantly enhancing cycle life to nearly 80% capacity retention after 500 cycles at 1C (Fig. 7a–c).[102] Embedding Fe–N_4 sites within N-doped hollow carbon spheres (Fe–N_4@hollow carbon) creates mesoporous catalytic shells that immobilize LiPSs and catalyze their rapid conversion within the confined space, enabling 77% capacity retention in Li–S pouch cells after 200 cycles (less than 50% for non-catalytic control, Fig. 7d–g).[103] Addressing the substantial 80% volume changes inherent to sulfur electrochemistry, emerging strategies focus on nano-stress regulation using flexible host frameworks, a key aspect of functional coupling.[73] Flexible polymer network hosts or lithiophilic fibrous carbon matrices that can dynamically adjust their pore structure or morphology accommodate volume expansion while maintaining essential interfacial contact and electronic/ionic connectivity. Embedding SACs within such adaptive frameworks, like Fe single atoms in a bacterial cellulose-templated host, ensures sustained catalytic activity and structural integrity, delivering ultralow capacity decay per cycle even at a high sulfur loading of 5 mg cm^{-2} (Fig. 7h–j).[102,104] Furthermore, the inherent porosity of optimized scaffolds (*e.g.*, biotemplated porous carbon, 3D hollow C_3N_4) maximizes electrolyte infiltration and Li^+ diffusion pathways, ensuring efficient access to SAC active sites and mitigating local concentration polarization.[104] Architectures like Ni single atoms anchored on hollow carbon nanosheets leverage these properties to achieve efficient bidirectional catalysis (facilitating both Li_2S formation and oxidation), enabling high sulfur utilization (1200 mA h g^{-1}, 72%) and stability even under elevated sulfur loading of nearly 7 mg cm^{-2} (Fig. 7k–n).[105,106]

3.3 Device-level integration: hierarchical control across scales

The precision catalysis paradigm culminates at the device level through the integration of multi-functional components that synergistically implement spatial configuration engineering, reaction pathway engineering, and functional coupling across the entire battery system. Designing bifunctional electrodes or separators that address both cathode and anode challenges simultaneously exemplifies this systemic approach. The "Janus" separator concept is a prime example. Conventional Celgard separators permit soluble polysulfides to shuttle to the lithium anode, forming insulating Li_2S_2 and Li_2S that reduce sulfur utilization and increase polarization *via* anode passivation. Simultaneously, inhomogeneous lithium stripping/plating generates dendrites that: (i) expose fresh surfaces to electrolyte decomposition, increasing resistance; (ii) form "dead" Li when disconnected by SEI films; and (iii) risk separator penetration causing short circuits. Coating one side (cathode-facing) with catalytic SAC layers, such as MOF-derived Co–O_4 nanosheets (Fig. 8a–c),[107] this separator simultaneously suppresses these issues: its Co–O_4 moieties chemically anchor polysulfides through Lewis acid–base interactions while homogenizing Li^+ flux *via* adsorption at oxygen sites, and its high Young's modulus physically blocks dendrite penetration, thus reducing capacity fade to an ultralow 0.07% per cycle. At the same time, a carbonized bio-MOF providing Zn–N_4 sites formed a thin coating that maintained ultra-low voltage polarization ($\Delta V \approx 30$ mV) for over 4000 hours by effectively anchoring polysulfides and regulating Li^+ flux (Fig. 8d and e).[108] Coating the opposite side (anode-facing) with lithiophilic SACs, like Ru–O_4 on carbon nanofibers (Ru–O_4@CNF) or Co–N_x on porous carbon nanofibers (Co–PCNF, Fig. 8f and g),[109] regulated Li^+ flux and guided uniform Li deposition, enabling symmetric Li‖Li battery stability for 400 hours (60 hours for the Celgard separator), effectively inhibiting dendrite growth (Fig. 9a–c).[110] This creates a robust interlinked cathode–anode protection mechanism, embodying functional coupling at the system level.

However, care must be taken with any catalyst applied to the Li-metal anode. While such lithiophilic coatings can promote uniform plating, they could *unintentionally accelerate* the corrosive reaction between migrating polysulfides and the

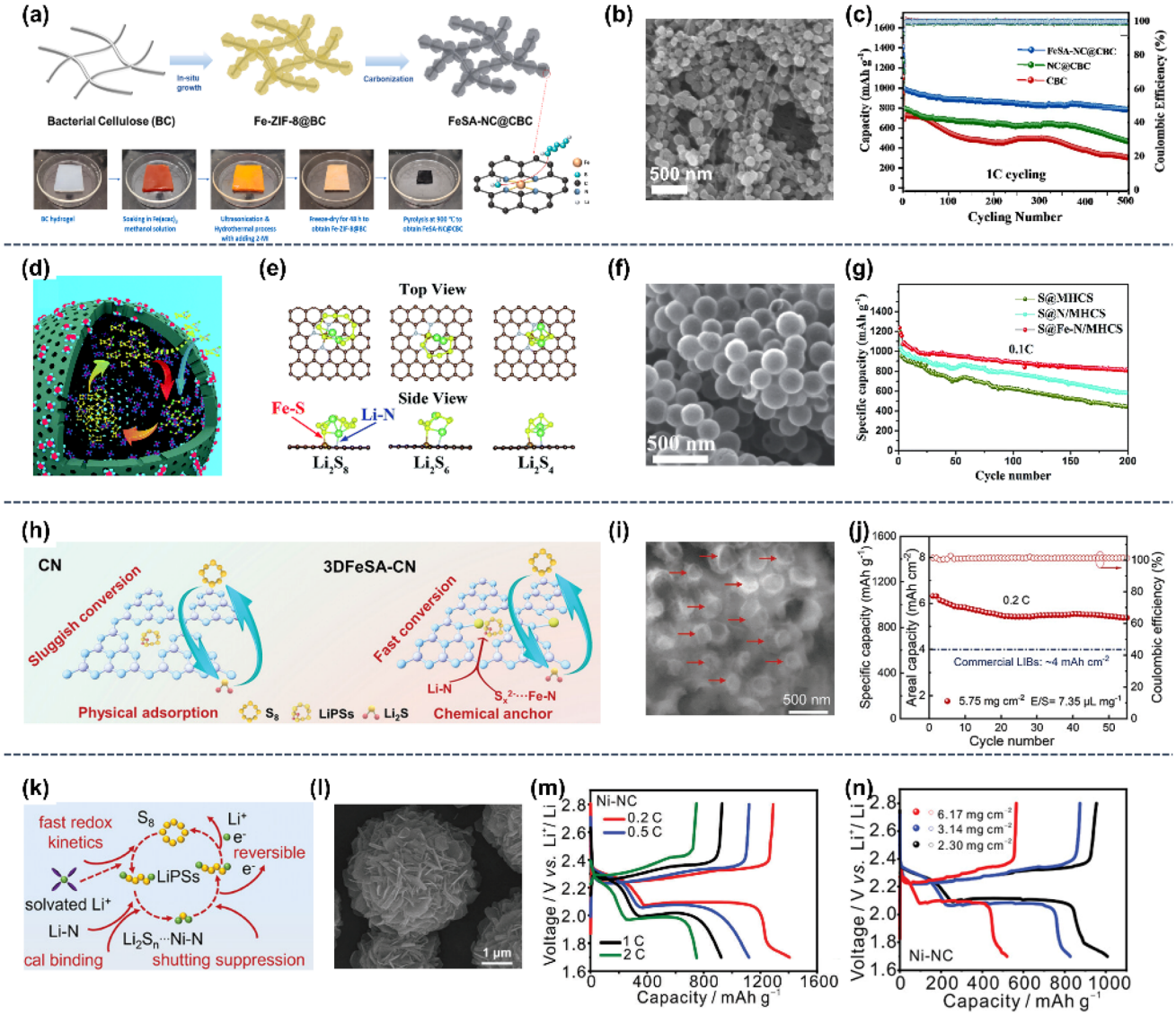

Fig. 7 Structural engineering of SAC–carbon frameworks for sulfur cathode optimization. (a) Schematic of FeSA–NC@CBC synthesis and corresponding digital photographs of Fe-ZIF-8@BC and FeSA–NC@CBC preparation procedures. (b) SEM images of FeSA–NC@CBC. (c) Cycling performance of the FeSA–NC@CBC-based battery with 5 mg cm^{-2} sulfur loading. Reproduced from ref. 102 with permission from Elsevier, Copyright 2023. (d) Schematic of Fe–N_4-embedded Fe–N/MHCS nanoreactors as sulfur cathode electrocatalysts. (e) Optimized configurations of polysulfides adsorbed on Fe–N_4–C with lowest energy states. (f) SEM images of Fe–N/MHCS. (g) Cycling stability of Fe–N/MHCS-based batteries at 0.1C. Reproduced from ref. 103 with permission from the Royal Society of Chemistry, Copyright 2020. (h) Schematic of polysulfide adsorption/conversion on CN and 3DFeSA-CN matrices. (i) SEM images of 3DFeSA-CN. (j) Cycling performance of 3DFeSA-CN-based batteries at 0.2C. Reproduced from ref. 104 with permission from Wiley-VCH GmbH, Copyright 2022. (k) Mechanism illustration of LiPS adsorption and conversion on Ni–NC. (l) SEM image of Ni–NC. (m) Charge–discharge voltage profiles of Ni–NC-based batteries at 0.2, 0.5, 1, 2, and 4C. (n) Charge–discharge voltage profiles at 0.1C under sulfur loadings of 2.30, 3.14, and 6.17 mg cm^{-2}. Reproduced from ref. 106 with permission from Wiley-VCH GmbH, Copyright 2023.

lithium surface if they also catalyze Li_2S formation at the anode. In other words, a poorly selective anode-side catalyst might exacerbate Li consumption by lowering the barrier for parasitic Li_2S deposition on the anode. To avoid this, anode SACs should be designed to catalyze only beneficial processes (*e.g.*, SEI stabilization or polysulfide *oxidation* back to sulfur) and remain inert to direct LiPS reduction. Strategies such as pairing the catalyst with $LiNO_3$ electrolyte additives or using SACs that preferentially mediate LiPS oxidation can help prevent runaway anode corrosion.[111]

Extending beyond single-site designs, multi-atom catalytic configurations leverage cooperative effects for enhanced reaction pathway engineering. Theoretical studies suggest that paired metal atoms (dual-atom catalysts, Fe–M DACs) can outperform isolated single atoms in LiPS conversion kinetics by providing complementary adsorption/catalysis sites. Crystal orbital Hamilton population (COHP) analysis of adsorbed Li_2S_4 on Fe/M–NC catalysts revealed weaker Li–S bonding in Fe/V–NC (indicated by lower-intensity negative/positive COHP and a smaller −ICOHP value), which manifests as reduced Li–S

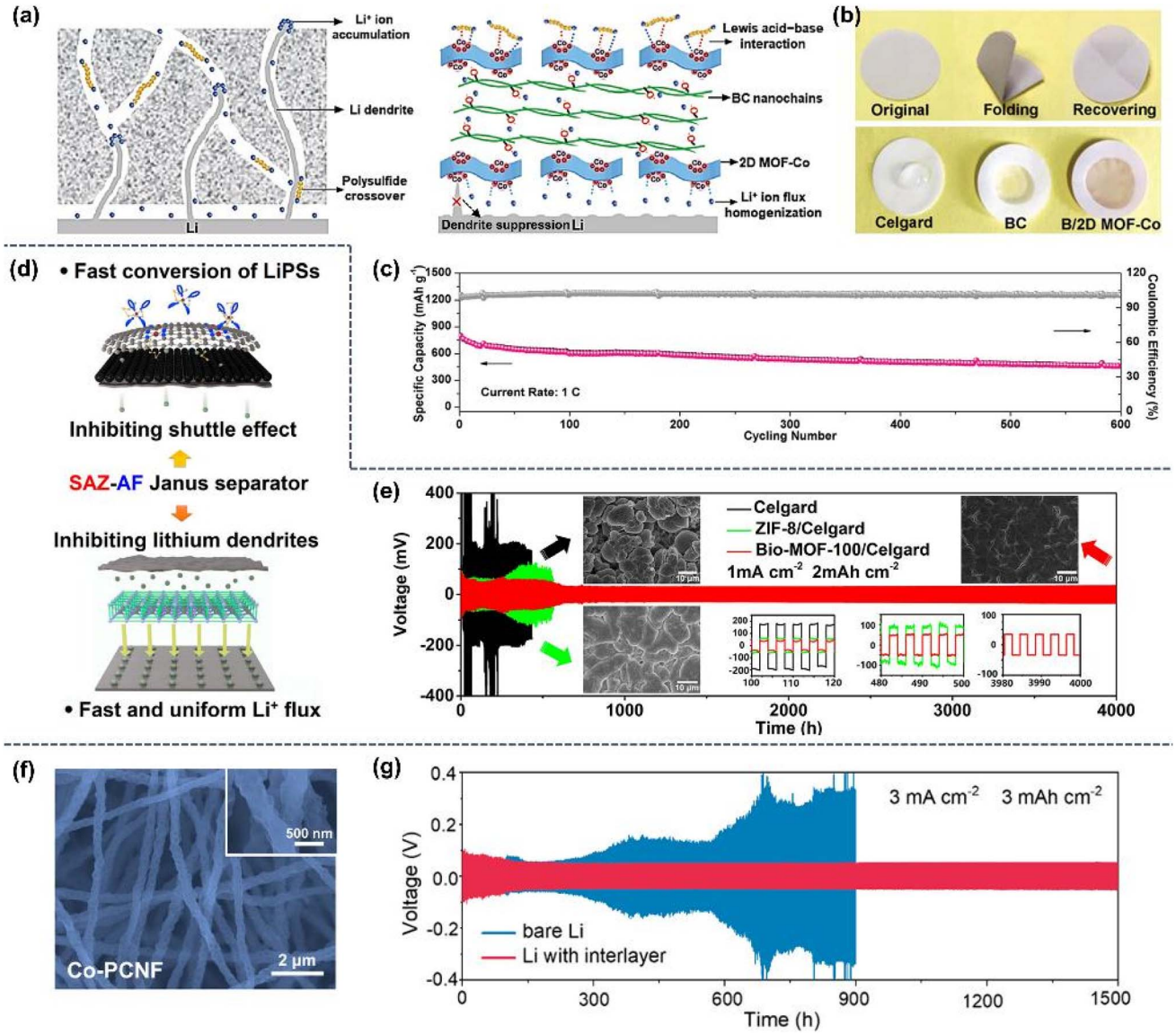

Fig. 8 Separator engineering for stabilizing Li metal and suppressing the shuttle effect. (a) Schematic of Li–S batteries assembled with Celgard and B/2D MOF-Co separators. (b) Flexibility and electrolyte wettability comparison of Celgard, BC, and B/2D MOF-Co separators. (c) Long-term cycling stability of Li–S batteries with a B/2D MOF-Co separator at 1C. Reproduced from ref. 107 with permission from Wiley-VCH GmbH, Copyright 2020. (d) Schematic of the SAZ-AF Janus separator for dendrite suppression and shuttle inhibition. (e) Li plating/stripping performance of symmetric batteries (2 mA h cm^{-2}, 1 mA cm^{-2}) over 4000 h using Celgard, ZIF-8/Celgard, and Bio-MOF-100/Celgard separators. Inset: SEM images of Li metal surfaces after cycling. Reproduced from ref. 108 with permission from the American Chemical Society, Copyright 2021. (f) SEM images of Co–PCNF. (g) Galvanostatic cycling of symmetric batteries at 3.0 mA cm^{-2} and 3.0 mA h cm^{-2} capacity. Reproduced from ref. 109 with permission from the American Chemical Society, Copyright 2021.

bond energy. The −ICOHP values of the Li–S bond show a linear increase from Fe/V–NC to Fe/Ni–NC, correlating with decreasing sulfur conversion efficiency, demonstrating Fe/V–NC's superior catalytic activity for Li_2S_4 conversion (Fig. 9d–f).[112] Experimentally, dual single-atom sites combining Pt and Co demonstrated an enhancement in sulfur redox kinetics and prolonged battery lifespan to 500 cycles compared to single-metal SACs.[113] Tandem catalysis represents another powerful strategy, integrating distinct but complementary active sites within a single structure (*e.g.*, atomic Fe–N_4 sites alongside Fe_3C nanoparticles) to concurrently accelerate sequential steps like Li^+ desolvation and sulfur conversion, dramatically improving high-rate capability to deliver 651 mA h g^{-1} at 3C (Fig. 9g and h).[114] Furthermore, controlled aggregation of single atoms into small clusters can leverage inter-atom synergy; for instance, tiny Zn atom clusters exhibited faster polysulfide conversion kinetics than isolated Zn atoms, further enhancing overall battery performance.[115] Looking towards future advancements, the integration of functional coupling principles paves the way for adaptive and intelligent systems. Concepts like "stress-gating" separator layers (using piezo-responsive materials to convert the pressure from volume changes into a catalytic activation signal) or light-

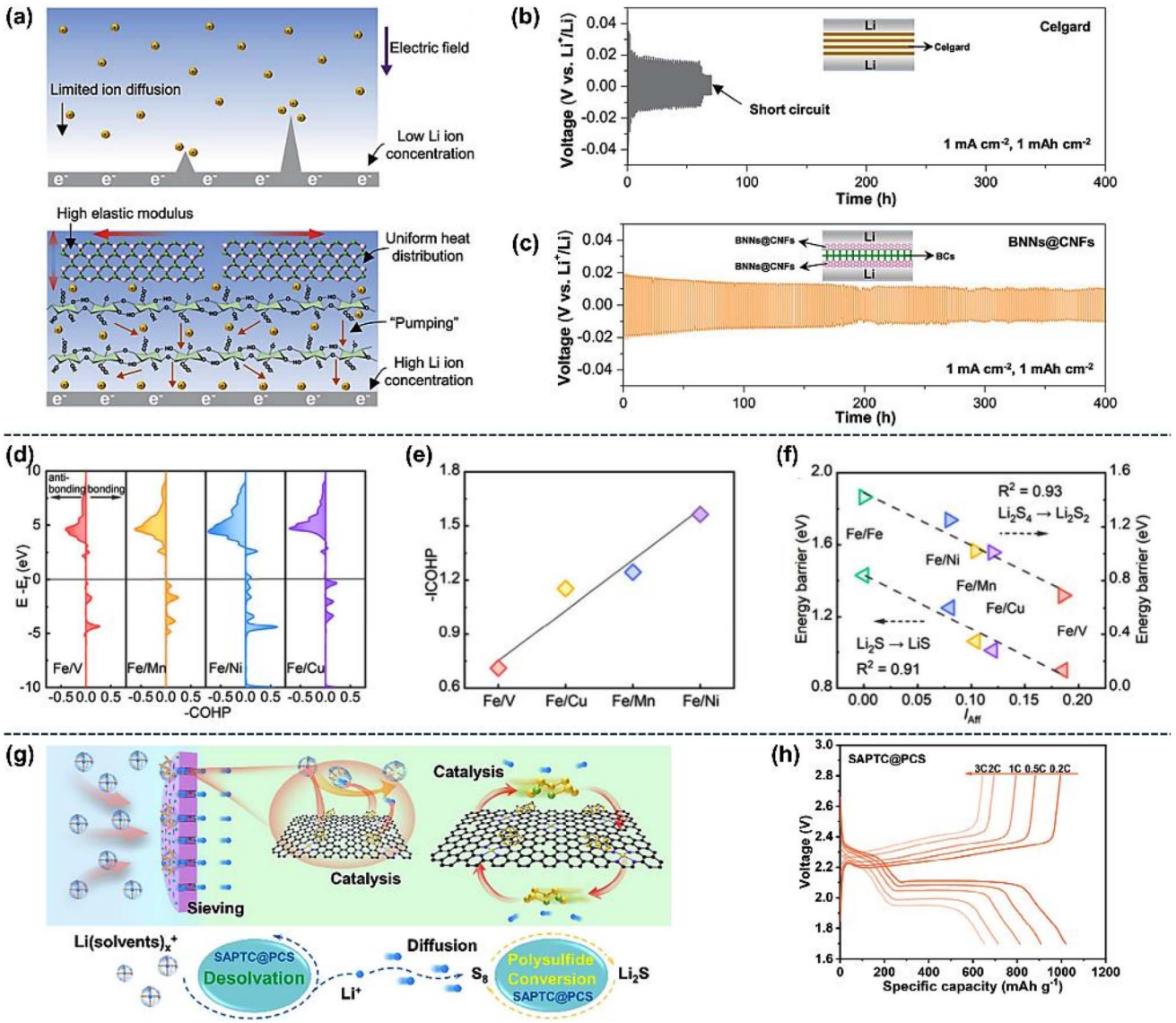

Fig. 9 Interfacial regulation and electronic descriptor analysis in Li–S batteries. (a) Schematic of BNNs@CNFs membrane for Li-metal protection. (b) Cycling stability of Li||Li symmetric batteries with a Celgard-based membrane. (c) Cycling stability with a BNNs@CNFs-based membrane. Reproduced from ref. 110 with permission from Wiley-VCH GmbH, Copyright 2022. (d) COHP diagram for the Li–S bond on Fe/M–NC. (e) Corresponding −ICOHP values. (f) Correlation between electron affinity index (I_{EA}) and energy barrier for Li_2S_4/Li_2S conversion. Reproduced from ref. 112 with permission from the American Chemical Society, Copyright 2024. (g) Schematic of Li^+ desolvation catalyzed by SAPTC@PCS. (h) Voltage–capacity profiles at various current rates. Reproduced from ref. 114 with permission from Wiley-VCH GmbH, Copyright 2025.

responsive SAC heterostructures represent frontier strategies for real-time, feedback-enabled reaction modulation.[80] Integrating such responsive elements with advanced *in situ* diagnostics could enable intelligent "catalyst-battery" networks capable of self-optimization based on operational conditions.

3.4 Realization pathways: from conceptual design to material fabrication

Translating the design principles of Sections 3.1–3.3 into high-performance Li–S batteries relies on innovative material synthesis and integration techniques. Key strategies include constructing SACs through MOF-derived frameworks, designing hollow carbon scaffolds for efficient sulfur hosting, and developing interface-adaptive architectures. MOF-derived SACs offer a versatile and powerful approach. MOFs serve as ideal precursors to synthesize SACs with atomic precision and tunable coordination. Pyrolysis of bimetallic MOFs (*e.g.*, Zn/Co-ZIF) allows volatile Zn evaporation, leaving transition metal atoms (Co, Fe, Ni, *etc.*) anchored as M–N_x sites within N-doped porous carbon matrices, achieving high densities of active sites per gram as exemplified by CoSA–HC with hierarchical porosity.[116,117] Coordination control is key; for instance, one such Fe–N–C cathode delivered higher capacities by virtue of its dense population of active Fe sites facilitating sulfur conversion.[117] MOF-derived SACs (*e.g.*, Fe–N–C, Co–N–C) can be integrated as catalytic additives in composite cathodes or coated

Table 1 Summary of representative SAC systems in Li–S batteries

Catalyst	Synthesis method	Test conditions (S loading/E/S)	Performance	Ref
Coordination-engineered SACs				
Mo–N–CNF	Hydrothermal and annealing	5.1 mg cm^{-2}	1248 mA h g^{-1} at 0.2C 715 mA h g^{-1} at 5C	36
Co–BN–G	One-pot hydrothermal	5.5 mg cm^{-2}/10 μL mg^{-1}	1034 mA h g^{-1} at 0.5C 851 mA h g^{-1} at 2C	37
CoSAC/CNT	Pyrolysis, adsorption and polymerization	2–7 mg cm^{-2}	990 mA h g^{-1} after 1000 cycles 4.1 mA h cm^{-2} at 7 mg cm^{-2}	40
CNT@f-CoNC	Schiff base reaction (no pyrolysis)	6.9 mg cm^{-2}/4 μL mg^{-1}	7.7 mA h cm^{-2} 90% retention/300 cycles	41
HP-SAFEs	Pyrolysis on porous carbon	1–4.1 mg cm^{-2}	Fe–N_4: 578 mA h g^{-1} Co–N_4: 512 mA h g^{-1} Ni–N_4: 454 mA h g^{-1}	45
Fe–N_3C_2–C	Coordination engineering	6.6 mg cm^{-2}/8 μL mg^{-1}	6.1 mA h cm^{-2} stable 1000 cycles	46
CoSA–N_3PS	Two-step self-templated pyrolysis	4.1 mg cm^{-2}	619 mA h g^{-1} at 10C 6.8 mA h cm^{-2} at 0.2C	56
Fe–N_2/NC	Pyrolysis	5.0 mg cm^{-2}/5.3 μL mg^{-1}	5.7 mA h cm^{-2} at 0.2C 1058/950/760 mA h g^{-1} at 1/2/5C	57
Ni–Fe–NC	MOF-derived pyrolysis	5.0 mg cm^{-2}/6 μL mg^{-1}	782 mA h g^{-1} at 0.5C/300 cycles	58
Fe–N_4/NC	Wet impregnation, pyrolysis and acid leach	Pouch: 8.4 mg cm^{-2}/3 μL mg^{-1} Coin: 2.0 mg cm^{-2}/10 μL mg^{-1}	1153/951 mA h g^{-1} at 0.05/0.2C 543 mA h g^{-1} at 5C	59
S–Co-SACs/NSC	Polymerization, pyrolysis and sulfurization	7.8 mg cm^{-2}/8 μL mg^{-1}	834 mA h g^{-1} at 5C 77.5% retention/500 cycles at 1C	60
Co-ACSA@NC	Pyrolysis	13.1 mg cm^{-2}/4 μL mg^{-1}	11.15 mA h cm^{-2} at 0.05C	66
Co–N_4/NC	Salt-template method	4.9 mg cm^{-2}	624 mA h g^{-1} at 5C	67
Mo–N_2C_1/C	MOF-derived pyrolysis	7.75 mg cm^{-2}/8 μL mg^{-1}	732 mA h g^{-1} at 10C	97
SACo@HC	One-step pyrolysis	5.4 mg cm^{-2}/4 μL mg^{-1}	1425 mA h g^{-1} at 0.05C 746 mA h g^{-1} at 4C	99
Fe,Co–NC	Pyrolysis and coordination control	1.2–8.0 mg cm^{-2}/5.2 μL mg^{-1}	1035 mA h g^{-1} at 0.1C 728 mA h g^{-1} at 4C	100
Zn–N_4–NC	ZIF-7 derived and pyrolysis	7.2 mg cm^{-2}/3.7 μL mg^{-1}	5.6 mA h cm^{-2} after 100 cycles 953 mA h g^{-1} (100 cycles, 0.1C)	115
FeSA-CN	Fe-ZIF-8 derived and pyrolysis	1.4 mg cm^{-2}/20 μL mg^{-1}	1123 mA h g^{-1} at 0.2C 605 mA h g^{-1} at 4C	117
Confined host architectures				
FeSA–NC@CBC	Fe-ZIF-8 derived and bacterial cellulose pyrolysis	2.5–5.0 mg cm^{-2}	840 mA h g^{-1} at 2C 800 mA h g^{-1} after 500 cycles at 1C	102
Fe–N/MHCS	MOF-assisted synthesis and pyrolysis	5.4 mg cm^{-2}/8 μL mg^{-1}	6.4 mA h cm^{-2} areal capacity 0.0187% fade/cycle (1000 cycles/1C)	103
3DFeSA-CN	Biotemplating and pyrolysis	5.75 mg cm^{-2}	6.18 mA h cm^{-2} at 5.75 mg cm^{-2}	104
SAPTC@PCS	Pyrolysis	6 mg cm^{-2}	804.8 mA h g^{-1} (100 cycles)	114
Device-level & functional coupling				
HD-V-SAC	*In situ* anchoring and pyrolysis	5.1 mg cm^{-2}	1144 mA h g^{-1} (0.5C) 76.3% retention/500 cycles	44
Co–N_3Cl_1	Inside-out two-step thermal reaction	7.5 mg cm^{-2}	804.3 mA h g^{-1} at 5C 0.023% per cycle (1000 cycles at 1C) 7.0 mA h cm^{-2} at $S \approx 7.5$ mg cm^{-2}	55
Co_{SAC}–NC	Template-assisted precursor infiltration, pyrolysis and template removal	0.9–3.1 mg cm^{-2}	650 mA h g^{-1} after 300 cycles/0.5C 473 mA h g^{-1} after 1000 cycles/1C 840 mA h g^{-1} after 100 cycles	63
Pt SAs/In_2S_3/Ti_3C_2	Ultrasound-assisted photochemical reduction	6.4 mg cm^{-2}	1068 mA h g^{-1} at 0.5C 720 mA h g^{-1} at 5C	80
Cu SA/N–$Ti_3C_2T_x$	Vacancy-assisted anchoring of asymmetric Cu–N_1C_2 sites	7.2 mg cm^{-2}/8 μL mg^{-1}	925 mA h g^{-1} at 3C 5.28 mA h cm^{-2}	98
Mn–N_3–Cl/BNC	Carbonization self-assembly	2.3 mg cm^{-2}	1384 mA h g^{-1} at 0.1C 743 mA h g^{-1} at 3C 0.06% fade/cycle over 700 cycles	101
Ni@NNC	*In situ* trapping in ZIF-8 and pyrolysis	4.85 mg cm^{-2}/8.4 μL mg^{-1}	1232.4 mA h g^{-1} at 0.3C 814.9 mA h g^{-1} at 3C	105

Table 1 (*Contd.*)

Catalyst	Synthesis method	Test conditions (S loading/E/S)	Performance	Ref
Ni–NC	Pyrolysis and adsorption	6.17 mg cm^{-2}	0.033% per cycle (700 cycles, 1C) 5.17 mA h cm^{-2} at 0.1C (≈300 cycles)	106
B/2D MOF-Co	Janus coating	7.8 mg cm^{-2}	0.07% per cycle (600 cycles) 5.0 mA h cm^{-2} at 7.8 mg cm^{-2}	107
SAZ-AF	MOF-derived Zn SAC	1.5–8.0 mg cm^{-2}/10 μL mg^{-1}	0.05% per cycle (1000 at 2C)	108
Co–PCNF	Electrospinning and pyrolysis	6.9 mg cm^{-2}/60 μL mg^{-1}	7.15 mA h cm^{-2} at 6.9 mg cm^{-2}/0.1C	109
BNNS@CNF	Interfacial engineering	5.8 mg cm^{-2}/3 μL mg^{-1}	460 mA h g^{-1} at 5C	110
Fe/V–NC	Pyrolysis anchoring	6.1 mg cm^{-2}/7.5 μL mg^{-1}	0.028% per cycle (1000 at 1C) 6.3 mA h cm^{-2} at 6.1 mg cm^{-2}	112
Pt&C@NCNT	Atomic layer deposition	2.5 mg cm^{-2}	822.1 mA h g^{-1} at 12.7 mA cm^{-2}	113
W–O_2N_2/NG	Self-template coating	8.3 mg cm^{-2}	678 mA h g^{-1} at 10C 605 mA h g^{-1} after 1000 cycles at 2C 6.24 mA h cm^{-2} at 8.3 mg cm^{-2}	120

onto separators/interlayers.[108,116–118] Combining SACs with hollow carbon structures (nanospheres, nanotubes, nanofibers) creates optimized catalytic nanoreactors. These provide void space for volume buffering, conductive pathways, high surface area (*e.g.*, 1281 m^2 g^{-1} for SiO_2-templated hollow spheres)[103] for SAC loading, and porous channels for electrolyte/Li^+ transport.[103,106,119] Techniques include templating (*e.g.*, SiO_2, bacterial cellulose),[102] vacuum-assisted layer-by-layer assembly (producing CNFs with interconnected channels),[110] and controlled carbonization. Fabricating components with inherent mechanical compliance or stimuli-responsiveness is crucial for functional precision. This involves designing flexible sulfur hosts, adaptive artificial SEI layers on Li anodes (*e.g.*, lithiophilic SACs embedded in porous carbon nanofiber films like Co–PCNF, featuring interwoven nanofibers with a diameter of ~300 nm, maintaining a stable Li nucleation overpotential of 10 mV at a current density of 1.0 mA cm^{-2} with a capacity of 1.0 mA h cm^{-2} and long cycleability for 1500 hours at 3.0 mA cm^{-2} under a capacity of 3.0 mA h cm^{-2}),[109] and multifunctional Janus separators/coatings.[107–110,118,120] Strategies include electrospinning, solution casting, vapor deposition, and *in situ* implantation techniques, such as trapping Ni atoms within S–C composites during cathode fabrication, enabling stable cycling at a high sulfur loading of 4.85 mg cm^{-2}.[105] Bifunctional interlayers, like those with Fe–N and Fe–O sites, effectively suppressed the shuttle effect to 0.045% capacity fade per cycle.[120]

Through this comprehensive multi-scale design philosophy, manipulating electronic states and local symmetry *via* atomic coordination engineering, creating tailored reaction microenvironments with porous, confining, and adaptive host architectures, and integrating multi-functional components at the device level, the precision catalysis theory is effectively materialized (detailed data shown in Table 1). This implementation not only validates the theoretical framework established in Chapter 2 but also provides the robust physicochemical foundation necessary for extending this paradigm to related systems (Na–S, K–S, Mg–S, leveraging their 2600 W h kg^{-1} theoretical energy density[5]) and solid-state configurations.

4. Multi-system extensions: broadening the scope of precision catalysis

While Li–S batteries provide a crucial foundation for single-atom catalyst (SAC) design and mechanistic understanding, significant differences in key parameters, such as ionic radius, electrode potential, polysulfide solubility, and deposit morphology, exist in other metal–sulfur systems (Na–S, K–S, Mg–S) and solid-state Li–S batteries. Consequently, precise catalytic strategies centered on spatial configuration engineering, reaction pathway engineering, and functional coupling require adaptation for each specific system.

4.1 Room-temperature Na–S and K–S batteries

Na–S and K–S systems share the conversion-type sulfur cathode with Li–S. However, larger cations (Na^+ radius: 1.02 Å *vs.* Li^+: 0.76 Å; K^+: 1.38 Å) and differing reactivities introduce distinct challenges.[121] Both systems form soluble polysulfide intermediates (Na_2S_n, K_2S_n), analogous to Li_2S_n, meaning the polysulfide shuttle effect remains problematic. Sodium polysulfides exhibit higher diffusivity, and the sodium anode's SEI is less robust, thereby exacerbating shuttling in Na–S batteries. To address this, SACs can mitigate this through strong chemisorption of sodium polysulfides (NaPSs), mirroring their action on LiPSs. Computational studies confirm that SAC motifs effective for Li–S (*e.g.*, Mo–N–C or Co–N–C sites) also bind NaPSs strongly, thus reducing shuttling. Mechanistically, incorporating Mo_{SAC} elevates d-band centers and modifies coordination environments in MoS_2, enabling site-specific orbital interactions that weaken S–S bonds and accelerate sulfur chain dissociation. Critically, this mechanism enhances

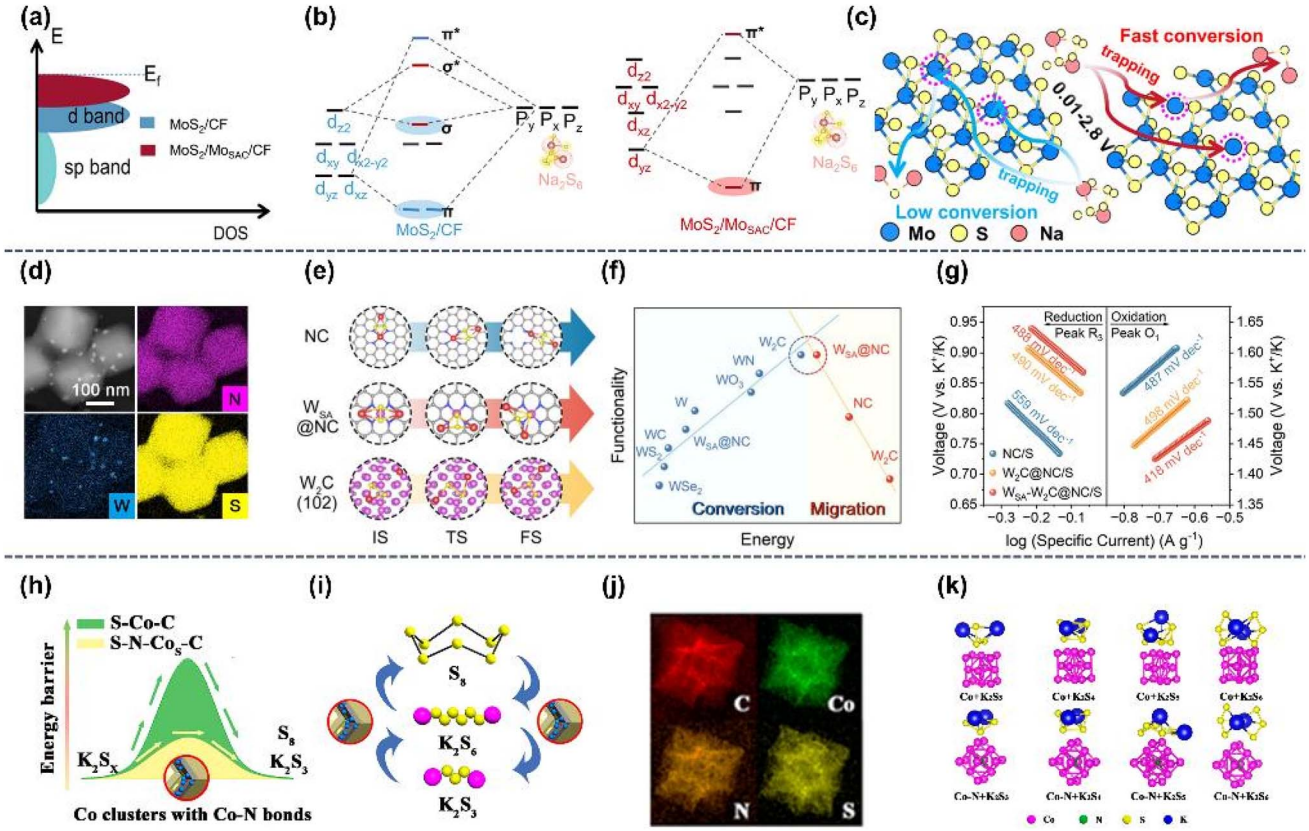

Fig. 10 Orbital modulation and catalytic design in Na/K–S battery systems. (a) Schematic of d-orbital energy level elevation. (b) Illustration of the d–p orbital hybridization scenario. (c) Schematic of electrochemical catalysis in room-temperature Na–S batteries. Reproduced from ref. 122 with permission from the American Chemical Society, Copyright 2024. (d) HAADF-STEM image and corresponding EDS mapping of W_{SA}-W_2C@NC/S. (e) Calculated initial, transition, and final states for K_2S_2 migration. (f) Volcano plot correlating KPS conversion/migration functionalities with specific energy. (g) Tafel slope of R_3 and O_1 peaks extracted from CV curves at 0.2 mV s^{-1}. Reproduced from ref. 124. Published by Springer Nature under a Creative Commons CC BY 4.0 license. (h and i) Schematic of the catalytic mechanism for S–N–Co_s–C Polyhedra. (j) Elemental mapping of S–N–Co_s–C polyhedra. (k) Optimized adsorption geometries of K_2S_3, K_2S_4, K_2S_5, and K_2S_6 on Co and N-doped Co nanoparticles. Reproduced from ref. 126 with permission from the American Chemical Society, Copyright 2020.

NaPS reduction kinetics in room-temperature Na–S batteries (Fig. 10a–c).[122]

Beyond shuttling, sluggish kinetics pose a major additional challenge: the larger bare ionic radii of Na^+ and K^+ lead to stronger solvent interactions and larger solvated ion sizes, resulting in slower diffusion and charge transfer. This kinetic limitation is especially acute in K–S systems, where discharge often terminates at non-stoichiometric K_2S_x ($x > 1$, *e.g.*, $K_2S_{0.8}$) rather than fully forming K_2S, primarily due to insurmountable barriers in the solid–solid conversion of K_2S_2 to K_2S.[123] Consequently, catalytic acceleration of this step is imperative.

To overcome these specific K–S solid-state conversion barriers, a dual-function catalyst was developed that synergistically facilitates potassium polysulfide (KPS) migration and catalyzed KPS conversion.[124] Theoretical calculations reveal a volcano-type relationship governing performance, with optimal activity achieved using W_2C nanocrystals and tungsten single atoms (W_{SA}) as dual-functional components. In this targeted design, W_2C acts as a catalytic site for KPS conversion and W_{SA}-modified carbon substrates serve as transport highways. This synergy concurrently addresses two key issues including sulfur-catalyst distribution mismatches by efficient KPS feeding to catalytic sites and catalytic poisoning by accelerating solid-state KPS migration. Crucially, W_{SA} lowers the K_2S migration energy barrier on carbon, facilitating mass transfer around W_2C sites. Without W_{SA}, sluggish product transport causes insulating KPS accumulation (*e.g.*, K_2S_2) that poisons catalytic sites (Fig. 10d–g).

Significant progress has also been achieved with other S_{AC} metals, notably atomic Co and Fe catalysts for Na–S/K–S. Zhang *et al.* decorated hollow carbon nanospheres with atomic Co for a Na–S cathode, achieving efficient electrocatalytic reduction of Na_2S_6 to solid Na_2S. This Co_{SA} design strongly anchored NaPSs and mitigated the higher overpotentials characteristic of Na–S systems, improving capacity and stability.[125] Similarly, in K–S batteries, Ge *et al.* utilized N-doped carbon derived from ZIF-67 loaded with atomic Co (N–Co_m–C) as a sulfur host; it provided strong KPS adsorption and catalyzed sluggish conversion steps, enabling higher sulfur utilization (Fig. 10h–k).[126] Importantly, the porous carbon matrix accommodated the larger space requirement for K^+ diffusion, while single Co sites facilitated the formation of end products closer to fully reduced K_2S.

Notably, the operating voltages of K–S and Na–S differ slightly ($K/K^+ \approx 2.93$ V *vs.* SHE, $Na/Na^+ \approx 2.71$ V *vs.* SHE), yet SACs demonstrate adaptability provided the catalyst remains stable in the respective electrolyte.[127] Future efforts integrating SACs onto tailored supports (*e.g.*, MXenes, metal chalcogenides, or 3D carbons) hold promise for boosting Na–S and K–S kinetics, which suffer from slower kinetics and more severe polysulfide shuttling than Li–S. For instance, a recent Na–S

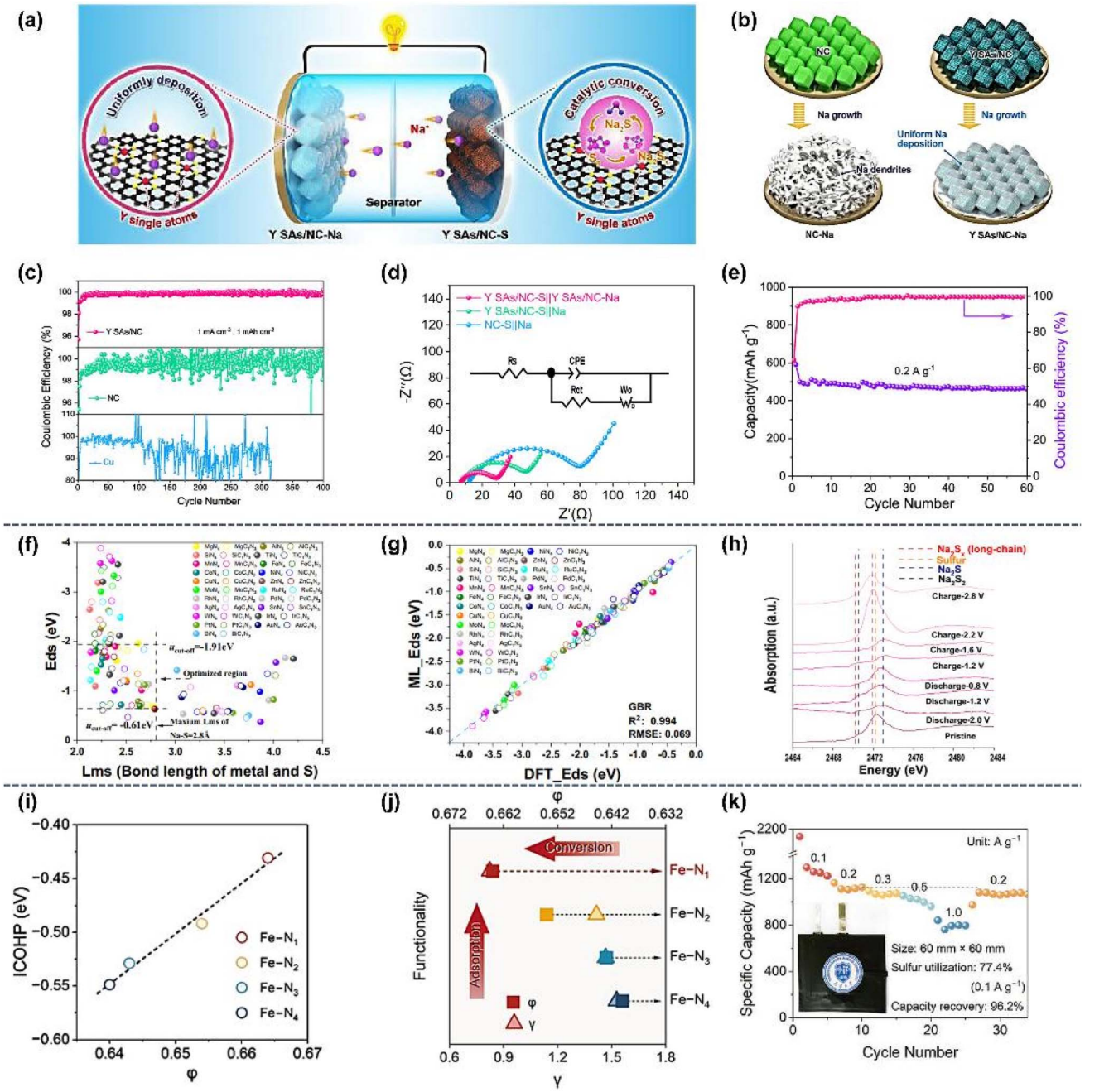

Fig. 11 Full-cell design and descriptor-guided catalysis in Na–S batteries. (a) Schematic of Y SAs/NC-S||Y SAs/NC-Na full cell configuration. (b) Schematic of Na plating behaviors on NC and Y SAs/NC electrodes. (c) Coulombic efficiencies of different electrodes at 1.0 mA h cm^{-2} deposition capacity and 1 mA cm^{-2} current density. (d) EIS spectra of Y SAs/NC-S||Y SAs/NC-Na, Y SAs/NC-S||Na, and NC-S||Na full cells. (e) Cyclic performance of the Na–S pouch cell (6 × 6 cm^2; 2.3 mg cm^{-2} S loading; E/S ratio, 4 μL mg^{-1}) at 0.2 A g^{-1}. Reproduced from ref. 128 with permission from the American Chemical Society, Copyright 2022. (f) Correlations between adsorption energy (E_{ds}) and metal–S bond length (L_{ms}). (g) Comparison of DFT-derived and machine-learning (gradient boosted regression, GBR)-predicted E_{ds} values. (h) *Ex situ* X-ray absorption spectra of S in S@Mn_1-PNC during the initial cycle. Reproduced from ref. 129 with permission from Springer Nature, Copyright 2024. (i) Relationship between the ICOHP values of Na–S bonds in Na_2S and electronic structure descriptor φ ($\varphi = e_g/t_{2g}$). (j) Schematic of Fe–N_x structures with high unsaturation for sulfur redox in Na||S batteries, based on geometric/electronic descriptors. (k) Rate performance of the Na||S pouch cell using an Fe–N_1/S cathode. Reproduced from ref. 130 with permission from Springer Nature, Copyright 2025.

cathode employed a Janus architecture coated with single-atom yttrium catalysts acting simultaneously on the sodium anode and the sulfur cathode. This bifunctional configuration significantly enhanced cycling stability by concurrently improving electrocatalytic polysulfide conversion and enabling reversible uniform Na deposition. Specifically, YN_4 sites enabled dendritic-free Na deposition (>99% coulombic efficiency over 400 cycles), lowered charge transfer resistance (22.7 Ω), and delivered 500 mA h g^{-1} at 0.2 A g^{-1} in ∼80 mg S pouch cells under lean electrolyte (Fig. 11a–e).[128] Supporting this, fundamental studies indicate that single-atom sites markedly enhance charge transfer at the Na–S cathode interface, accelerating overall reaction kinetics (Fig. 11f–h).[129]

Complementary to experimental approaches, machine learning identifies metal–sulfur bond length as a critical descriptor for adsorption energy, aligning with DFT calculations to reveal a linear relationship between E_{ads} and SACs. This enables rapid screening of optimal SACs (Mn–N_4, Fe–N_4, Rh–N_4, Mg–N_4, Co–N_4, Mg–C_1N_3) within a specific bond length region favoring mild polysulfide adsorption. Building on this screening, a "single-atom charging strategy" addresses sulfur's intrinsic poor conductivity (which causes incomplete reactions and metastable products). Atomic manganese sites demonstrate enhanced electron capture/donation capability, establishing synergistic adsorption–electron transfer that selectively promotes short-chain sodium polysulfides. Concurrently, charge transfer facilitates sodium ion rearrangement *via* electrostatic forces, accelerating ion kinetics while improving pathway selectivity and stable product formation. These combined mechanisms collectively enhance room-temperature sodium–sulfur battery performance.

Beyond Co, coordinatively unsaturated Fe–N_x single-atom sites have proven highly effective for Na–S. A strategic sulfur host design employs unsaturated Fe–N_x sites, introducing dual activity descriptors: the geometric parameter γ (l_{Na-S}/l_{Fe-N}) and the electronic parameter φ (e_g/t_{2g}) both correlate with the Fe–N_x unsaturation degree. Theoretical calculations establish that γ negatively correlates with sodium polysulfide adsorption strength, while φ positively correlates with Na_2S decomposition capability. Consequently, Fe–N_1 sites, exhibiting minimal γ and maximal φ, are identified as optimal for polysulfide behavior regulation. Experimentally, the Fe–N_x catalyst delivered 1297 mA h g^{-1} (77.4% sulfur utilization) at 0.1 A g^{-1} in a Na–S pouch cell, alongside excellent high-rate performance in a coin cell (1003 mA h g^{-1} at 1.675 A g^{-1}) and prolonged cycling stability (83.5% capacity retention over 450 cycles at 3.35 A g^{-1}, Fig. 11i–k).[130]

4.2 Mg–S batteries

Magnesium–sulfur batteries involve divalent Mg^{2+}, fundamentally altering the electrochemistry compared to monovalent systems. While Mg–S batteries offer high theoretical energy density (Mg provides 2 electrons per ion), they suffer from high polarization and sluggish kinetics due to strong Mg^{2+}–solvent interactions and the tendency to form passivating MgS (Fig. 12a).[131] Specifically, Mg^{2+} has a smaller ionic radius (0.72 Å) but double the charge, leading to slow diffusion and poor conductivity in MgS.[132] Furthermore, common electrolytes are often incompatible with Mg metal and dissolved polysulfides. Consequently, Mg–S reactions frequently stall, resulting in low capacity and rapid fade.

Catalysts play a decisive role in overcoming these challenges by lowering kinetic barriers and modifying reaction pathways. A major bottleneck is the re-oxidation of solid MgS during charging, a process associated with a large overpotential. Studies confirm that adding catalysts like TiS_2 to the sulfur cathode accelerates the conversion of MgS back to higher polysulfides, thereby alleviating capacity decay.[133] Similarly, Co-based sulfide catalysts on MXene improve performance; for instance, a Co_3S_4@MXene/S composite cathode delivered 1220 mA h g^{-1} with good stability. Mechanistically, the Co_3S_4 and conductive MXene provide dual functions: chemisorbing polysulfides and catalyzing Mg^{2+} insertion/extraction.[134]

SACs for Mg–S represent an emerging but promising strategy. Given the strong polar Mg–S bonds, highly polar SAC sites (*e.g.*, O-coordinated single atoms or fluorine-doped environments) might facilitate Mg–S bond breaking. While direct Mg–S SAC reports are currently limited, insights can be extrapolated from Li/Na systems; for example, isolated Cu–N/O single sites derived from MOFs promote conversion between short-chain polysulfides and Na_2S in Na–S batteries.[135] Analogously, introducing SACs with mixed N/O coordination in Mg–S cathodes could help form a more conductive MgS_x intermediate layer, facilitating dissolution and reformation. Critically, the multi-electron nature of Mg–S demands catalysts capable of managing complex electron transfer. SACs with variable valence (*e.g.*, single-atom V, Ti, or Mo) might be particularly advantageous. Supporting this, *in situ* XAS studies by Xu *et al.*[136] and Zhao-Karger *et al.*[137] confirmed that Mg–S discharge involves multi-step solid-state conversions, and that appropriate catalysts significantly reduce the activation energy of these steps. Fundamentally, SACs offer the potential to tune the surface energy and adsorption properties of MgS, promoting its formation in a more amorphous and reversible manner.

Indeed, preliminary SAC studies show significant promise for Mg–S batteries. Specifically, a carbon host decorated with isolated Fe–N–C sites significantly lowered the overpotential and delivered higher discharge capacities compared to an uncatalyzed cathode.[138] Furthermore, to address polarization holistically, a "self-tandem" catalyst design was introduced, wherein one component accelerates Mg^{2+} desolvation at the anode and another catalyzes sulfur conversion at the cathode, collectively reducing polarization and improving overall Mg–S kinetics (Fig. 12b–d).[139] Building on this concept, the STAR@LCNC modified Mg–S battery establishes a cross-linked conductive network with strong MgS_x adsorption and accelerated conversion kinetics *via* atomic reactor promoters, enabling high-rate capability and extended lifespan across varied mass loadings. Notably, at a high sulfur loading of 4 mg cm^{-2}, this battery delivers an initial capacity of 964 mA h g^{-1} (0.1C). After 50 cycles, it maintains 75.6% capacity retention with a high areal capacity of 2.92 mA h cm^{-2}, performance unmatched in previous low/high-loading Mg–S systems.

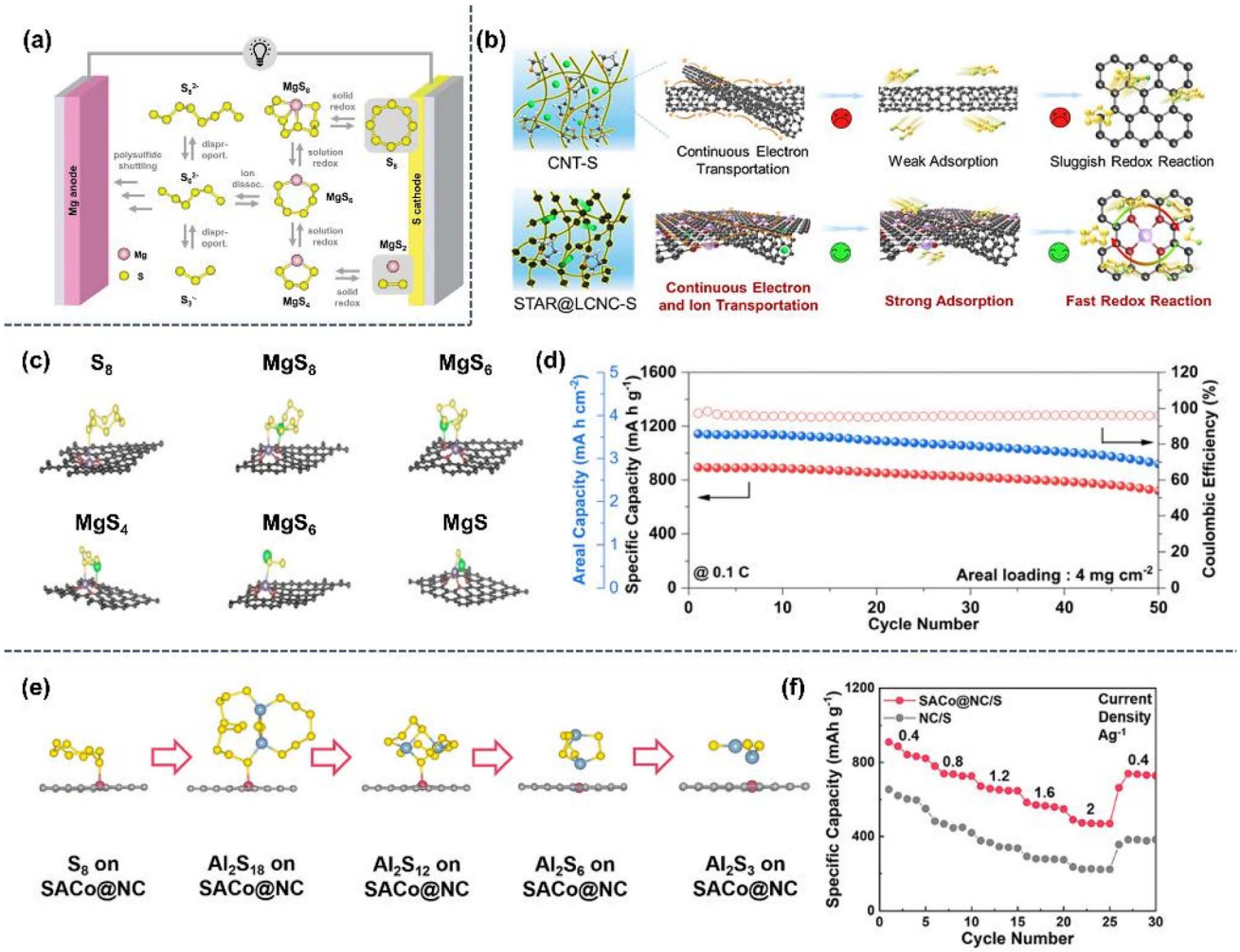

Fig. 12 Single-atom catalysis for polysulfide regulation in Mg/Al–S battery systems. (a) Summary of the current understanding of polysulfide behavior in Mg–S battery systems. Reproduced from ref. 131 with permission from Wiley-VCH GmbH, Copyright 2024. (b) The proposed catalytic mechanism without atomic reactors in CNT-S or with STAR@LCNC-S in Mg–S batteries. (c) The corresponding structure illustrations of different S_8, MgS_8, MgS_6, MgS_4, MgS_2 and MgS on STAR@LCNC and carbon substrates. (d) The high mass loading STAR@LCNC-S electrode cycled at 0.1C. Reproduced from ref. 139 with permission from the Royal Society of Chemistry, Copyright 2024. (e) Optimized configurations of S_8, Al_2S_{18}, Al_2S_{12}, Al_2S_6 and Al_2S_3 adsorption on SACo@NC. (f) Rate performance of SACo@NC/S and NC/S cathodes. Reproduced from ref. 140 with permission from Elsevier, Copyright 2022.

In summary, while Mg–S batteries are currently limited by electrolyte issues, SACs represent a promising route to catalyze sulfur conversion and help realize high theoretical capacity by specifically overcoming kinetic bottlenecks. This potential extends beyond Mg–S; preliminary studies on aluminum–sulfur batteries also suggest SACs can boost sulfur conversion, hinting at the broad applicability of precise catalysis across diverse multivalent metal–sulfur chemistries (Fig. 12e and f).[140]

4.3 Solid-state and lean-electrolyte Li–S systems

Lean-electrolyte and all-solid-state Li–S batteries are actively pursued to enhance energy density and safety. However, minimizing or eliminating the liquid electrolyte exacerbates the sluggish sulfur conversion kinetics, as LiPS mobility is suppressed and solid–solid reactions dominate. Consequently, solid-state Li–S batteries often suffer from low sulfur utilization and high polarization, particularly at practical sulfur loadings.[141] Catalysis, especially leveraging spatial configuration engineering, is therefore crucial to mediate these challenging solid-phase transformations. As highlighted by Yang *et al.*, catalysts can effectively mitigate slow kinetics in both lean-electrolyte and solid-state Li–S batteries by providing alternative pathways and enabling Li_2S/Li_2S_2 nucleation with a lower overpotential (Fig. 13a and b).[142–144] Notably, under "dry" conditions with little or no free solvent, the most critical challenge is that polysulfide species cannot readily diffuse or shuttle. While this suppresses self-discharge, it also causes sulfur species to become trapped and reactions to stall. The localized electrolyte environment in lean systems is characterized by high viscosity and salt concentration, which hinders Li^+ diffusion and significantly increases polarization. As a result, lean-electrolyte cells often suffer from an early end of discharge,

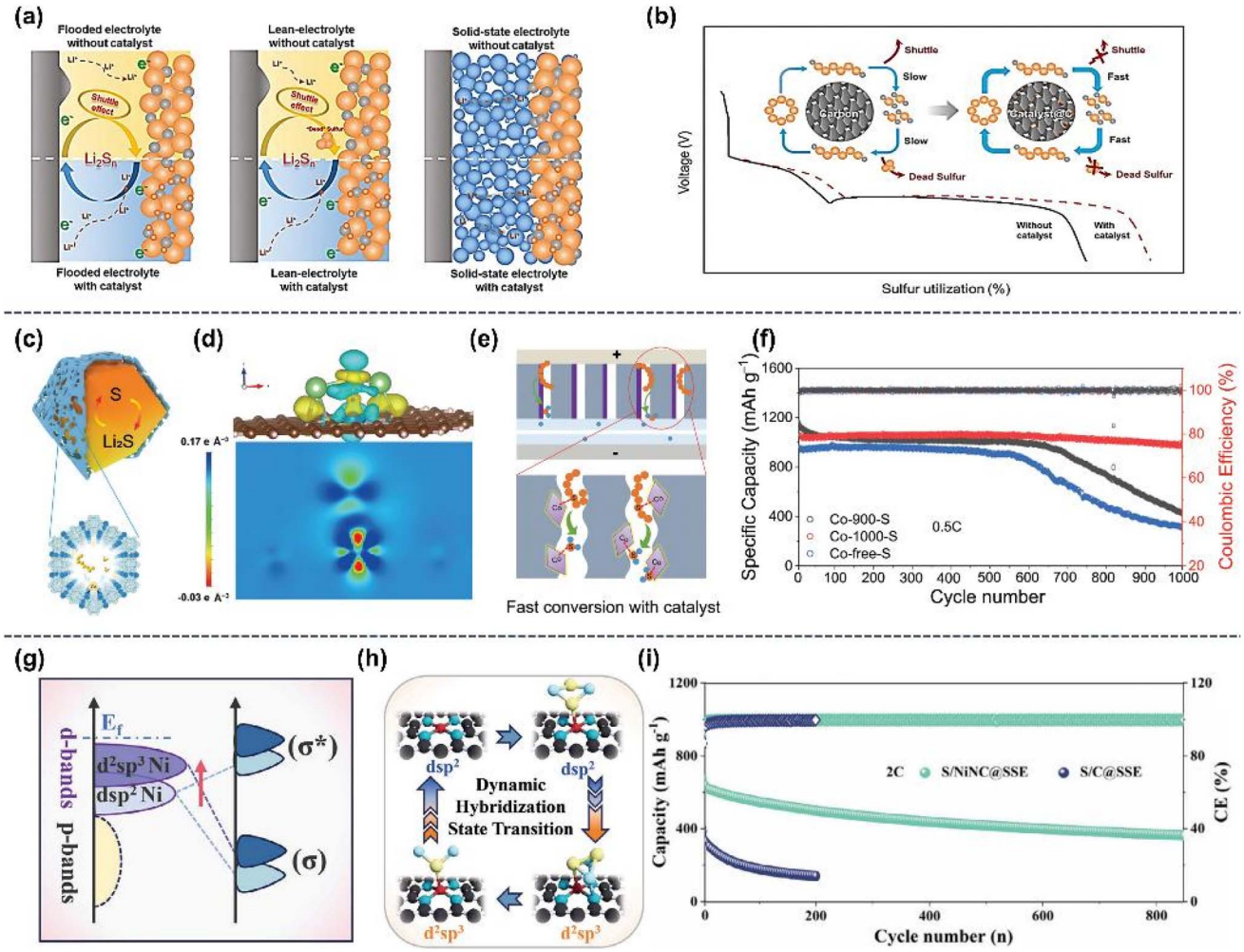

Fig. 13 Catalyst-driven sulfur conversion under electrolyte-constrained Li–S battery conditions. (a) Schematic of Li–S batteries with flooded, lean, and solid-state electrolytes. (b) Sulfur utilization in Li–S batteries with and without catalysts. Inset: catalytic process. Reproduced from ref. 142 with permission from Wiley-VCH GmbH, Copyright 2025. (c) Schematic of solid-state sulfur conversion confined in microporous channels. (d) Charge density difference of the Co-1000–Li_2S system. (e) Mechanism of sulfur conversion in Co-catalyzed micropore channels. (f) Cycling performance of batteries with different cathodes in a carbonate-based electrolyte at low sulfur loading at 0.5C. Reproduced from ref. 147 with permission from Wiley-VCH GmbH, Copyright 2024. (g) Shift in d-band center position after hybridization state transformation. (h) Schematic of dynamic hybridization state evolution of Li_2S_2 on NiNC. (i) Cycling performances of S/NiNC@SSE and S/C@SSE-based all-solid-state Li–S batteries at 2C. Reproduced from ref. 148 with permission from Wiley-VCH GmbH, Copyright 2025.

accumulation of insoluble Li_2S_2/Li_2S, and accelerated electrode passivation, ultimately leading to sluggish kinetics and incomplete sulfur utilization. In such scenarios, LiPS conversion may rely almost entirely on surface reactions, making catalytic interfaces indispensable. Under these conditions, SACs can act as local nano-reactors, catalyzing polysulfide conversion directly at the electrode–electrolyte interface and providing "micro-solvation" or alternative reaction pathways that alleviate kinetic bottlenecks. Accordingly, SAC design in lean-electrolyte systems should also prioritize shortening Li^+ transport pathways, for example, through porous conductive frameworks or interlayers, to further mitigate ion transport limitations.[145,146]

One strategy relying heavily on spatial configuration engineering confines sulfur within nanoporous carbon frameworks decorated with SACs, enabling short-range ion/electron transport even without liquid mediation. For instance, Yang *et al.* embedded sulfur within microporous carbon channels containing Co–N_4 single-atom sites (Fig. 13c–f).[147] In this design, sulfur directly contacts catalytic Co sites, enabling *in situ* "solid–solid" conversion to Li_2S_2/Li_2S during discharge without dissolution. This approach yielded high coulombic efficiency and significantly improved capacity retention (0.016% decay per cycle over 1000 cycles) in a polymer-electrolyte Li–S battery. Mechanistically, the catalyst likely lowers the interfacial energy for Li_2S formation, promoting uniform nucleation and growth instead of surface passivation. Similarly, coupling solid-state Li_2S with M–N_4 SACs (*e.g.*, Ni–N_4, Fe–N_4) has achieved remarkable rate capability and long cycle life, affirming SACs as transformative for solid-state Li–S. A notable example: a recent study using Ni–N_4 and Fe–N_4 SACs significantly enhanced the conversion kinetics of Li_2S_2 to Li_2S *via* reaction pathway engineering. Specifically, the elevated d-band center near E_F

populates antibonding orbitals, accelerating electron transfer during Li_2S_2 reduction. Furthermore, Ni–NC catalyzes this conversion *via* reversible hybridization switching: from the initial dsp^2 hybridization to d^2sp^3 upon Li_2S_2 adsorption, then back to dsp^2 after Li_2S formation, enabling rapid catalytic cycling. Consequently, the system achieved 1506 mA h g^{-1} at 0.05C and 70% capacity retention over 600 cycles at 2.0C in an all-solid-state battery (Fig. 13g–i).[148] Complementing this, another study utilizing Fe–N_4 motifs demonstrated exceptionally rapid Li_2S deposition kinetics in a comparable architecture, underscoring the efficacy of M–N_4 coordination sites.[45]

However, in the absence of the liquid electrolyte, active sites risk poisoning by immobile sulfur species; excessively strong binding of Li_2S_x on SACs can deactivate them over time.[64] This necessitates designing SACs with balanced interaction strengths (a critical aspect of spatial configuration engineering) to ensure continuous catalytic turnover. Likewise, under weakly solvating electrolyte (WSE) conditions, typically formulated using fluorinated or bulky solvents or high salt concentrations to reduce polysulfide solubility, LiPSs remain largely in the solid or aggregated form, significantly slowing their reaction kinetics. While this greatly suppresses polysulfide crossover and mitigates the shuttle effect, it also makes conversion kinetics more sluggish. In such WSE-based Li–S cells, SACs become even more crucial: they must actively facilitate polysulfide transformations that would otherwise proceed through solution-mediated pathways. Accordingly, catalysts must function effectively at solid electrolyte interfaces, capturing and activating sparsely solvated polysulfide species. Design principles for SACs under WSE conditions therefore emphasize highly accessible active sites and multifunctional character, for example, single-atom sites that can both strongly adsorb polysulfides and catalyze their reduction efficiently, thereby compensating for the loss of solvent mediation. Recent kinetic studies have identified Li_2S nucleation as a potential rate-limiting step in WSE systems; in particular, the direct solid-phase conversion of Li_2S_2 to Li_2S often becomes the key bottleneck. SACs that provide nucleation templates or lower the barrier for this transformation have demonstrated improved rate performance in lean/WSE-based cells.[149–151]

Embedding sulfur in SAC-decorated nanoporous carbon matrices, a core spatial configuration engineering tactic, effectively creates short-range transport pathways. Beyond improving kinetics, these matrices compensate for the lack of liquid-phase mediation by providing catalytically active surfaces that mimic solution-like transport, facilitating electron and ion movement at solid–solid interfaces. They also mitigate interfacial contact issues: SAC-embedded conductive matrices bridge sulfur particles and solid electrolytes, ensuring continuous pathways.[152] The emerging "catalyst as an integrator" concept highlights this advantage: coating solid electrolytes or sulfur cathodes with thin SAC-containing layers accommodates

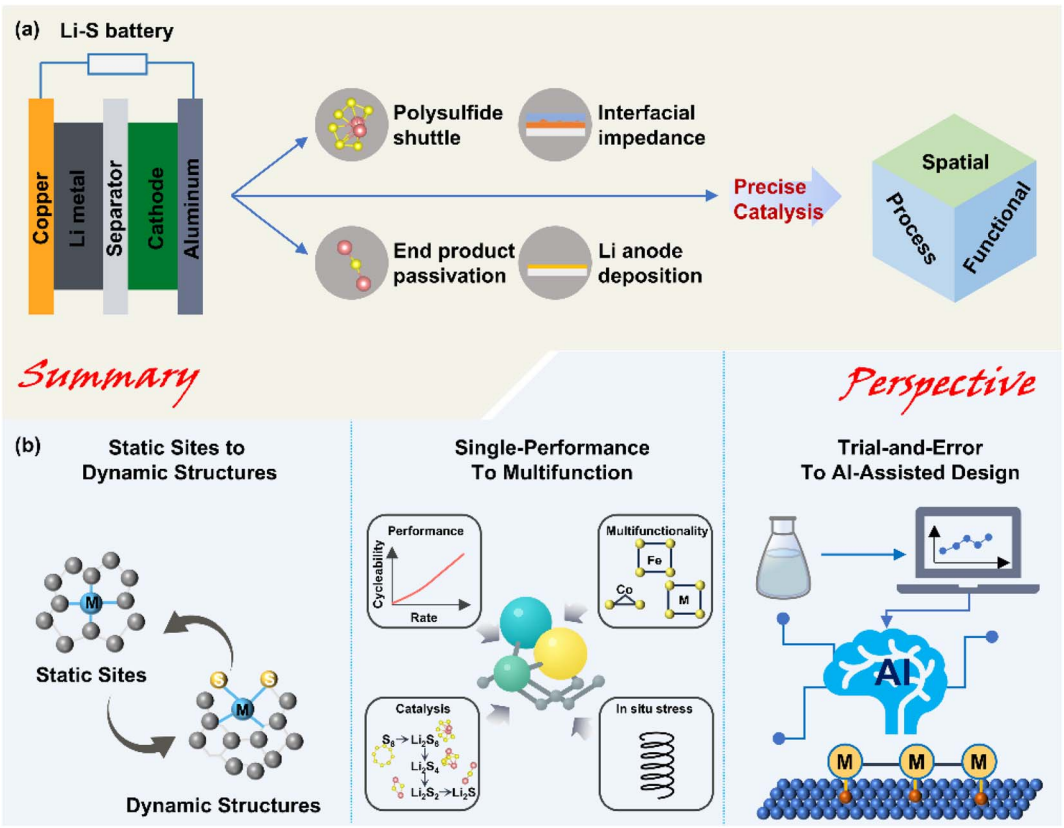

Fig. 14 Summary and prospects of precision catalysis in SAC-regulated Li–S batteries. (a) Summary of SAC applications in Li–S batteries and the proposed logic of precision catalysis across spatial, process, and functional dimensions. (b) Outlook on the evolution of SACs: from static to dynamic sites, from single-function to multifunctional synergy, and from empirical design to AI-assisted development.

volume changes (functional coupling) while maintaining robust interfacial contact.[153]

Previously, improving sulfur kinetics in solid-state configurations received little emphasis. Recent studies conclusively demonstrate that heterogeneous catalysts (*e.g.*, SACs, nanoalloys) dramatically improve sulfur utilization and rate capability. As Yang *et al.* conclude,[142] the judicious application of catalysts in lean and solid-state setups, particularly through spatial configuration engineering and reaction pathway engineering, can "propel the practical adoption" of these high-energy designs. Future design principles for SACs in solid/lean-electrolyte Li–S will focus on ensuring ionic percolation (*e.g.*, *via* hybrid ion-conductive scaffolds, spatial configuration), thermal stability (considering potential elevated operating temperatures), and multi-functionality (catalyzing sulfur reactions while potentially aiding Li plating at the anode *via* functional coupling). The inherent strengths of SACs, near 100% active site utilization, tunable chemistry, and adaptability, make them exceptionally well-suited for meeting these engineering needs. Ultimately, the synergy of solid electrolytes (eliminating external shuttling) and SACs (accelerating internal kinetics *via* spatial configuration and reaction pathway engineering) holds promise for all-solid-state Li–S batteries achieving high energy density without sacrificing power or lifespan.

5. Conclusion and outlook: the next frontier for SACs and the future of precise catalysis

Li–S batteries, with their high theoretical energy density and abundant resource base, remain pivotal candidates for next-generation energy storage. However, persistent challenges including polysulfide shuttling, interfacial impedance, and Li_2S passivation have hindered practical deployment. Against this backdrop, SACs leverage maximized atom utilization and tunable electronic structures to deliver superior reaction-regulation capabilities beyond conventional catalysts. Centered on the paradigm of "precision catalysis" (Fig. 14a), this review has systematically established a spatial-process-functional triaxial framework for SACs, elucidating their mechanistic roles in: (i) shuttle suppression *via* confinement and adsorption engineering (spatial configuration engineering); (ii) multi-step pathway modulation through kinetic barrier control (reaction pathway engineering); (iii) deposition behavior optimization *via* nucleation site regulation (functional coupling). Building on this foundation, we further translated this paradigm into scalable material design strategies, from atomic microenvironment engineering to device-level heterostructure integration, and extended its applicability to Na/K/Mg–S and solid-state systems. Collectively, our analysis validates that single-atom precision can fundamentally reconfigure Li–S electrochemistry, thereby establishing the proposed framework as a transformative design principle.

Nonetheless, it is important to recognize that catalysts operate within the bounds of thermodynamics. Electrocatalysis can accelerate reaction kinetics and lower overpotentials, but it cannot overcome the fundamental free-energy landscape of the Li–S chemistry. For instance, there are intrinsic equilibrium potentials and phase stabilities (defined by ΔG) that set the theoretical limits for Li_2S conversion and polysulfide formation. SACs can help the system approach these thermodynamic limits more efficiently, but they cannot shift an equilibrium beyond what thermodynamics allows. This means that even with "perfect" catalysts, certain voltage plateaus or capacity ceilings (*e.g.*, complete utilization of sulfur or 100% Li_2S reoxidation) are ultimately dictated by thermodynamic factors. As highlighted by recent phase equilibrium studies of Li–S, future catalyst design should work in concert with favorable thermodynamic pathways, stabilizing intermediate states only to the extent that it does not introduce prohibitive thermodynamic penalties. In short, precision catalysis must be cognizant of the thermodynamic boundaries of the Li–S system, ensuring that kinetic enhancements align with what is thermodynamically achievable.[154]

Looking ahead, we envision transformative shifts in four core aspects of Li–S research, intrinsically linked to the spatial configuration engineering, reaction pathway engineering, and functional coupling paradigm:

5.1 Evolving from static sites to dynamic structures in spatial configuration engineering

Growing experimental evidence (especially *in situ* characterization) indicates significant reconstruction of SAC coordination environments and electronic states during cycling. This dynamic evolution presents both a challenge (instability) and an opportunity (adaptive catalysis). Therefore, developing SAC architectures with intrinsic reconstruction responsiveness, exemplified by reversible switching between coordination modes ($M–N_4$ and $M–S_x$), will be critical for enhancing long-term stability and compatibility across all Li–S reaction stages.

5.2 Advancing from single-performance enhancement to system-level multifunctionality *via* functional coupling

While most current SAC designs focus on improving isolated metrics (rate, cycle life), practical Li–S demands holistic system-level functionality. Future innovations could include catalysts that are responsive to compressive stress from volume expansion or "self-sensing" catalytic systems that provide online diagnostic signals *via* interfacial electronic feedback. Future efforts could integrate piezoelectric or thermoelectric components with SACs, leveraging extreme volume changes as regulation signals to dynamically modulate catalytic pathways (reaction pathway engineering). This would enable "intelligent" reaction control that adapts in real time (functional coupling).

5.3 Accelerating discovery with AI-assisted catalyst design for spatial, pathway, and functional optimization

AI and high-throughput computation will fundamentally reshape SAC research. Machine learning can rapidly map electronic structure–activity relationships and predict optimal catalyst parameters (metal type, coordination, and support

properties for spatial configuration engineering), dramatically accelerating discovery *versus* trial-and-error. Building on predictive discovery, exemplified by Lian *et al.*'s machine learning (graph neural networks and Bayesian optimization) guided design of SAC cathodes using DFT-calculated binding energies[155] and computational screening identifying Mo/W-graphene's exceptional activity for Li_2S oxidation (reaction pathway engineering) later validated experimentally. AI's role is expanding beyond initial catalyst identification. Crucially, it now enables optimization of catalyst structures (*e.g.*, tailoring ligand arrangements for target binding energies *via* spatial configuration engineering) and real-time battery management (*e.g.*, dynamically adjusting charging protocols based on catalyst-state feedback, embodying functional coupling). This progression culminates in the ultimate vision of autonomous reaction regulation: closed-loop systems where catalysts, materials, and algorithms co-optimize continuously. Early manifestations include autonomous labs employing robotics/ML for material optimization and algorithms that iteratively "learn" ideal conditions, dynamically tuning sulfur loading, electrolyte amount, or SAC doping while integrating *in situ* diagnostic feedback (Fig. 14b), to maximize system-level performance.

5.4 From laboratory prototypes to industrial-scale implementation

Scalability and long-term stability remain critical bottlenecks for translating SACs from laboratory demonstrations to practical Li–S batteries. Producing SACs in large quantity with consistent atomic dispersion is inherently non-trivial: most reported synthesis routes, such as MOF-derived pyrolysis, wet-impregnation followed by high-temperature activation, or templating, are optimized only at gram or sub-gram scales. Scaling these methods to kilogram-level production introduces challenges in precursor cost, structural uniformity, and process control. To address this, researchers are exploring continuous processes such as roll-to-roll deposition of single-atom coatings or high-throughput flame spray pyrolysis, which promise throughput and reproducibility. Emerging approaches including monolithic SAC architectures, high-temperature atom trapping, and electrochemical dispersion of bulk metals to single atoms also illustrate that scalable, manufacturing-friendly routes are actively being pursued. A consistent theme is the need to maintain atomic dispersion at higher loadings, since single atoms risk clustering if temperature, atmosphere, or reduction environments are not rigorously controlled.

Equally important is the long-term stability of SACs under extended cycling. While SACs often show superior initial performance due to maximized active-site exposure, their stability is closely tied to the strength of metal–support interactions. Thermodynamically, isolated atoms are mobile and can gradually aggregate if defect sites are saturated or if harsh operating conditions (high current densities, elevated temperatures) induce atom migration. To mitigate this, strategies such as dopant engineering, strong anchoring *via* nitrogen/oxygen coordination, and the use of covalent organic frameworks have been employed to immobilize single atoms. Moreover, some SACs exhibit reversible coordination dynamics (*e.g.*, M–N to M–S transitions) during cycling; when harnessed, these dynamic structural changes can sustain activity rather than cause deactivation.

Moving forward, robust validation protocols, including long-term cycling over hundreds to thousands of cycles, high-loading cathodes, and pouch-cell demonstrations, are essential to confirm stability. In addition, composite architectures that integrate SACs with conductive, volume-accommodating frameworks can buffer mechanical stress while preserving catalytic activity. By explicitly addressing scalable synthesis and cycling durability, we provide a frank perspective on what it will take to move SACs toward real-world application. Overcoming these hurdles, achieving uniform dispersion at scale, designing stable anchoring environments, and validating performance in realistic device settings will be key to unlocking the transformative potential of SACs in practical Li–S batteries.

Overall, precise catalysis with single-atom catalysts, grounded in spatial configuration engineering, reaction pathway engineering, and functional coupling, is redefining the way we approach Li–S batteries, shifting the focus from treating symptoms to proactively controlling reaction pathways. By integrating atomic-level catalyst design with intelligent regulation and cross-disciplinary innovations, we can pave the way for Li–S and related systems to achieve unprecedented performance, stability, and functionality. The insights and frameworks presented here lay the foundation for future breakthroughs, heralding a new paradigm where single atoms serve not just as passive additives, but as active, programmable agents of electrochemical transformation, an outlook holding immense promise for revolutionizing multi-electron energy storage.

Author contributions

All authors contributed to the conceptualization, literature analysis, and writing of this review manuscript.

Conflicts of interest

The authors declare no competing interests.

Data availability

The copyrights for data supporting this review article have been obtained.

Acknowledgements

This work was supported by the A*STAR RIE 2025 Manufacturing Trade and Connectivity (MTC) Programmatic Fund (M24N6b0043) administered by A*STAR.

References

1 P. F. Sang, Q. L. Chen, D. Y. Wang, W. Guo and Y. Z. Fu, *Chem. Rev.*, 2023, **123**, 1262–1326.

2 Z. Li, J. T. Zhang, Y. M. Chen, J. Li and X. W. Lou, *Nat. Commun.*, 2015, **6**, 8850.
3 J. Y. Li, L. Gao, F. Y. Pan, C. Gong, L. M. Sun, H. Gao, J. Q. Zhang, Y. F. Zhao, G. X. Wang and H. Liu, *Nano-Micro Lett.*, 2024, **16**, 12.
4 S. H. Chung and A. Manthiram, *Adv. Mater.*, 2019, **31**, 1901125.
5 C. Huang, J. Xiao, Y. Y. Shao, J. M. Zheng, W. D. Bennett, D. P. Lu, L. V. Saraf, M. Engelhard, L. W. Ji, J. G. Zhang, X. L. Li, G. L. Graff and J. Liu, *Nat. Commun.*, 2014, **5**, 3015.
6 L. K. J. Ting, Y. Gao, H. M. Wang, T. Wang, J. G. Sun and J. Wang, *ACS Omega*, 2022, **7**, 40682–40700.
7 X. H. Zhao, X. Y. Wu, Q. Q. Hao, Y. S. Liu, K. X. Wang and J. S. Chen, *ACS Appl. Mater. Interfaces*, 2024, **16**, 63647–63654.
8 W. Q. Yao, J. Xu, L. B. Ma, X. M. Lu, D. Luo, J. Qian, L. Zhan, I. Manke, C. Yang, P. Adelhelm and R. J. Chen, *Adv. Mater.*, 2023, **35**, 2212116.
9 M. Sadd, S. D. Angelis, S. Colding-Jørgensen, D. Blanchard, R. E. Johnsen, S. Sanna, E. Borisova, A. Matic and J. R. Bowen, *Adv. Energy Mater.*, 2022, **12**, 2103126.
10 S. F. Ng, M. Y. L. Lau and W. J. Ong, *Adv. Mater.*, 2021, **33**, 2008654.
11 C. Lu, Y. Chen, Y. Yang and X. Chen, *Nano Lett.*, 2020, **20**, 5522–5530.
12 W. Q. Song, C. X. Xiao, J. Ding, Z. C. Huang, X. Y. Yang, T. Zhang, D. Mitlin and W. B. Hu, *Adv. Mater.*, 2024, **36**, 2301477.
13 P. P. Cao, X. Q. Mu, F. J. Chen, S. C. Wang, Y. R. Liao, H. Liu, Y. P. Du, Y. X. Li, Y. D. Peng, M. Z. Gao, S. L. Li, D. S. Wang and Z. H. Dai, *Chem. Soc. Rev.*, 2025, **54**, 3848–3905.
14 Y. N. Shang, X. Xu, B. Y. Ga, S. B. Wang and X. G. Duan, *Chem. Soc. Rev.*, 2021, **50**, 5281–5322.
15 Z. Z. Du, X. J. Chen, W. Hu, C. H. Chuang, S. Xie, A. J. Hu, W. S. Yan, X. H. Kong, X. J. Wu, H. X. Ji and L. J. Wan, *J. Am. Chem. Soc.*, 2019, **141**, 3977–3985.
16 Y. C. Yang, Y. W. Yang, Z. X. Pei, K. H. Wu, C. H. Tan, H. Z. Wang, L. Wie, A. Mahmood, C. Yan, J. C. Dong, S. L. Zhao and Y. Chen, *Matter*, 2020, **3**, 1442–1476.
17 G. F. Dai, S. Z. Li, M. L. Shi, L. X. Sun, Y. Jiang, K. N. Hui and Z. Q. Ye, *Adv. Funct. Mater.*, 2024, **34**, 2315563.
18 Y. F. Zhao, W. J. Jiang, J. Q. Zhang, E. C. Lovell, R. Amal, Z. J. Han and X. Y. Lu, *Adv. Mater.*, 2021, **33**, 2102801.
19 J. D. Shen, Z. W. Liang, T. T. Gu, Z. Y. Sun, Y. W. Wu, X. Q. Liu, J. H. Liu, X. Y. Zhang, J. W. Liu, L. Shen, M. Zhu and J. Liu, *Energy Environ. Sci.*, 2024, **17**, 6034–6045.
20 S. C. Li, C. S. Cao, J. B. Chen, W. Wen, X. F. Zhang, L. J. Cui, Y. K. Li, X. Huang, Y. Tang and Z. L. Xie, *Nat. Commun.*, 2025, **16**, 5790.
21 H. Q. Wang, H. Y. Sui, Y. L. Ding, Y. Yang, Y. Q. Su and H. Li, *J. Am. Chem. Soc.*, 2025, **147**, 6095–6107.
22 J. Xu, X. X. Xue, G. L. Shao, C. F. Jing, S. Dai, K. He, P. P. Jia, S. Wang, Y. F. Yuan, J. Luo and J. Lu, *Nat. Commun.*, 2023, **14**, 7849.
23 W. Liu, R. Chen, Z. Y. Sang, Z. X. Li, J. H. Nie, L. C. Yin, F. Hou and J. Liang, *Adv. Mater.*, 2024, **36**, 2406403.
24 X. B. Yang, X. N. Li and Y. Q. Huang, *Front. Chem. Sci. Eng.*, 2024, **18**, 79.
25 B. Q. Wang, M. Wang, Z. T. Fan, C. Ma, S. B. Xi, L. Y. Chang, M. S. Zhang, N. Ling, Z. Y. Mi, S. H. Chen, W. R. Leow, J. Zhang, D. S. Wang and Y. W. Lum, *Nat. Commun.*, 2024, **15**, 1719.
26 Y. H. Pan, X. Z. Wang, W. Y. Zhang, L. Y. Tang, Z. Y. Mu, C. Liu, B. L. Tian, M. C. Fei, Y. M. Sun, H. H. Su, L. B. Gao, P. Wang, X. F. Duan, J. Ma and M. N. Ding, *Nat. Commun.*, 2022, **13**, 3063.
27 Y. Qin, J. Wen, L. R. Zheng, H. Y. Yan, L. Jiao, X. S. Wang, X. L. Cai, Y. Wu, G. J. Chen, L. J. Chen, L. Y. Hu, W. L. Gu and C. Z. Zhu, *Nano Lett.*, 2021, **21**, 1879–1887.
28 X. P. Gao and H. X. Yang, *Energy Environ. Sci.*, 2010, **3**, 174–189.
29 H. Yuan, H. J. Peng, J. Q. Huang and Q. Zhang, *Adv. Mater. Interfaces*, 2019, **6**, 1802046.
30 M. Helen, M. A. Reddy, T. Diemant, U. Golla-Schindler, R. J. Behm, U. Kaiser and M. Fichtner, *Sci. Rep.*, 2015, **5**, 12146.
31 H. L. Ye, J. G. Sun, S. L. Zhang, H. B. Lin, T. R. Zhang, Q. F. Yao and J. Y. Lee, *ACS Nano*, 2019, **13**, 14208–14216.
32 Y. C. Wang, F. L. Chu, J. Zeng, Q. J. Wang, T. Y. Naren, Y. Y. Li, Y. Cheng, Y. P. Lei and F. X. Wu, *ACS Nano*, 2021, **15**, 210–239.
33 K. Wang, S. Liu, Z. H. Shu, Q. Y. Zheng, M. S. Zhe and Q. F. Dong, *Phys. Chem. Chem. Phys.*, 2023, **25**, 25942.
34 H. R. Zhao, Y. Z. Song and J. Y. Sun, *Batteries Supercaps*, 2023, **6**, e202200494.
35 Q. P. Wu, X. J. Zhou, J. Xu, F. H. Cao and C. L. Li, *ACS Nano*, 2019, **13**, 9520–9532.
36 D. Y. Guo, X. Zhang, M. L. Liu, Z. S. Yu, X. A. Chen, B. Yang, Z. Zhou and S. Wang, *Adv. Funct. Mater.*, 2022, **32**, 2204458.
37 F. Wang, T. C. Wang, Z. H. Shi, S. R. Cui, N. Wang, G. H. Kang, G. Su, W. Liu and Y. C. Jin, *ACS Appl. Mater. Interfaces*, 2024, **16**, 55229.
38 Y. Gong, J. Li, K. Yang, S. Y. Li, M. Xu, G. P. Zhang, Y. Shi, Q. Cai, H. X. Li and Y. L. Zhao, *Nano-Micro Lett.*, 2023, **15**, 150.
39 R. Zhou, S. N. Gu, M. Guo, S. Z. Xu and G. W. Zhou, *Energy Environ. Mater.*, 2024, **7**, e12703.
40 K. A. Samawi, E. A. A. Salman, H. A. Hasan, H. M. A. Mahmoud, S. M. Mohealdeen, G. Abdulkareem-Alsultan, E. Abdulmalekf and M. F. Nassar, *Mol. Syst. Des. Eng.*, 2024, **9**, 464–476.
41 M. Li, H. Liu, H. F. Li, D. Y. Luan, Z. M. Liu and X. W. Lou, *Angew. Chem., Int. Ed.*, 2025, **64**, e202503174.
42 W. X. Xu, S. Y. Lang, K. Y. Wan, R. Zeng, H. Q. Li, X. R. Fen, M. R. Krumov, S. M. Bak, C. J. Pollock and H. D. Abruña, *Sci. Adv.*, 2023, **9**, eadi5108.
43 Z. L. Yi, F. Y. Su, L. Huo, G. Y. Cui, C. L. Zhang, P. D. Han, N. Dong and C. M. Chen, *Appl. Surf. Sci.*, 2020, **503**, 144446.
44 Q. Q. Chen, J. Gu, H. L. Huang, W. Wang, W. C. Zhang, S. Meng and L. F. Liu, *J. Mater. Chem. A*, 2025, **13**, 16958–16969.

45 R. Yan, Z. Y. Zhao, M. H. Cheng, Z. Yang, C. Cheng, X. K. Liu, B. Yin and S. Li, *Angew. Chem., Int. Ed.*, 2023, **135**, e202215414.
46 G. L. Liu, W. M. Wang, P. Zeng, C. Yuan, L. Wang, H. T. Li, H. Zhang, X. H. Sun, K. H. Dai, J. Mao, X. Li and L. Zhang, *Nano Lett.*, 2022, **22**, 6366–6374.
47 D. B. Seo, D. Kim, M. R. Kim, J. Kwon, H. J. Kook, S. Kang, S. Yim, S. S. Lee, D. O. Shin, K. S. An and S. Park, *Nano-Micro Lett.*, 2025, **17**, 224.
48 X. Jiao, X. X. Tang, J. R. Li, Y. J. Xiang, C. P. Li, C. Tong, M. H. Shao and Z. D. Wei, *Chem. Sci.*, 2024, **15**, 7949–7964.
49 S. R. Burse, H. B. Tyagaraj, M. Safarkhani, S. J. Marje, G. S. Kumar, A. A. Ghaferi, E. Alhajri, N. R. Chodankar, Y. S. Huh and Y. K. Han, *Adv. Compos. Hybrid Mater.*, 2025, **8**, 216.
50 Z. H. Zeng, W. Nong, Y. Li and C. X. Wang, *Adv. Sci.*, 2021, **8**, 2102809.
51 Z. H. Shen, X. Jin, J. M. Tian, M. Li, Y. F. Yuan, S. Zhang, S. S. Fang, X. Fan, W. G. Xu, H. Lu, J. Lu and H. G. Zhang, *Nat. Catal.*, 2022, **5**, 555–563.
52 X. Wang, X. M. Zhang, Y. Zhao, D. Luo, L. L. Shui, Y. B. Li, G. Ma, Y. J. Zhu, Y. G. Zhang, G. F. Zhou, A. P. Yu and Z. W. Chen, *Angew. Chem., Int. Ed.*, 2023, **62**, e202306901.
53 Z. J. Lao, Z. Y. Han, J. B. Ma, M. T. Zhang, X. R. Wu, Y. Y. Jia, R. H. Gao, Y. F. Zhu, X. Xiao, K. Yu and G. M. Zhou, *Adv. Mater.*, 2024, **36**, 2309024.
54 S. Y. Lang, S. H. Yu, X. R. Feng, M. R. Krumov and H. D. Abruña, *Nat. Commun.*, 2022, **13**, 4811.
55 F. L. Cao, X. K. Zhang, Z. H. Jin, J. Y. Zhang, Z. Y. Tian, D. B. Kong, Y. P. Li, Y. T. Li and L. J. Zhi, *Adv. Energy Mater.*, 2024, **14**, 2303893.
56 C. X. Dong, C. N. Ma, C. Zhou, Y. K. Yu, J. J. Wang, K. S. Yu, C. L. Shen, J. P. Gu, K. J. Yan, A. Q. Zheng, M. J. Gong, X. Xu and L. Q. Mai, *Adv. Mater.*, 2024, **36**, 2407070.
57 J. Y. Wang, W. B. Qiu, G. R. Li, J. B. Liu, D. Luo, Y. G. Zhang, Y. Zhao, G. F. Zhou, L. L. Shui, X. Wang and Z. W. Chen, *Energy Storage Mater.*, 2022, **46**, 269–277.
58 J. L. Yang, P. H. Yang, D. Q. Cai, Z. Wang and H. J. Fan, *Nano Lett.*, 2023, **23**, 4000–4007.
59 W. G. Lim, C. Y. Park, H. Jung, S. Kim, S. H. Kang, Y. G. Lee, Y. C. Jeong, S. B. Yang, K. Sohn, J. W. Han and J. Lee, *Adv. Mater.*, 2023, **35**, 2208999.
60 T. T. Sun, F. D. Huang, J. L. Liu, H. Yu, X. Y. Feng, X. F. Feng, Y. Yang, H. B. Shu and F. Q. Zhang, *Adv. Funct. Mater.*, 2023, **33**, 2306049.
61 J. C. Ren, J. W. Han, P. F. Yu, J. J. Zhou, T. Y. Ren, W. Liu and S. Li, *J. Phys. Chem. C*, 2023, **127**, 23156–23163.
62 Z. W. Liang, J. D. Shen, X. J. Xu, F. K. Li, J. Liu, B. Yuan, Y. Yu and M. Zhu, *Adv. Mater.*, 2022, **34**, 2200102.
63 W. H. Cao, M. Y. Liu, K. Zhang, S. H. Zhang, C. X. Li, Y. H. Wen, Q. L. Lv, Q. Wen and L. Wang, *J. Colloid Interface Sci.*, 2025, **684**, 189–196.
64 C. Li, H. B. Luo, F. Y. Li and F. Li, *ACS Omega*, 2023, **8**, 45348–45357.
65 X. H. Zhao, Y. J. Xu, T. Qiu, Y. K. Zhang, W. Z. Liu, C. Z. Chen, M. J. Biggs and C. Hu, *Energy Storage Mater.*, 2024, **72**, 103728.
66 J. B. Liu, X. Y. Zhang, H. Y. Li, S. F. Jia, J. H. Li, Q. Li, Y. G. Zhang and G. R. Li, *InfoMat*, 2025, **7**, e12649.
67 Y. J. Li, J. B. Wu, B. Zhang, W. Y. Wang, G. Q. Zhang, Z. W. Seh, N. Zhang, J. Sun, L. Huang, J. J. Jiang, J. Zhou and Y. M. Sun, *Energy Storage Mater.*, 2020, **30**, 250–259.
68 M. Zhao, H. J. Peng, B. Q. Li, X. Chen, J. Xie, X. Liu, Q. Zhang and J. Q. Huang, *Angew. Chem., Int. Ed.*, 2020, **59**, 9011–9017.
69 X. Y. Li, S. Feng, M. Zhao, C. X. Zhao, X. Chen, B. Q. Li, J. Q. Huang and Q. Zhang, *Angew. Chem., Int. Ed.*, 2022, **61**, e202114671.
70 X. Zhou, R. J. Meng, N. Zhong, S. F. Yin, G. Q. Ma and X. Liang, *Small Methods*, 2021, **5**, 2100571.
71 Y. T. Feng, L. H. Zu, S. S. Yang, L. Chen, K. X. Liao, S. Meng, C. Zhang and J. H. Yang, *Adv. Funct. Mater.*, 2022, **32**, 2207579.
72 R. Wang, J. L. Yang, X. Chen, Y. Zhao, W. G. Zhao, G. Y. Qian, S. N. Li, Y. G. Xiao, H. Chen, Y. S. Ye, G. M. Zhou and F. Pan, *Adv. Energy Mater.*, 2020, **10**, 1903550.
73 P. T. Xiao, F. X. Bu, G. H. Yang, Y. Zhang and Y. X. Xu, *Adv. Mater.*, 2017, **29**, 1703324.
74 K. Wang, Y. Wang, J. Wang, H. Wang, C. Z. Ding, Z. B. Zheng, Y. Liu, Z. T. Luo and Y. Ding, *Adv. Funct. Mater.*, 2025, **35**, 2422689.
75 W. J. Chen, Y. Yu, Y. Du, Y. Wang, Y. Zhao, K. Guo, P. F. Yuan, J. N. Zhang and G. Qu, *Adv. Mater.*, 2024, **36**, 2409369.
76 R. Xu, J. Ren, X. Y. Shen, Y. Zhu, Y. Shan and C. G. Shi, *ACS Omega*, 2022, **7**, 18826–18833.
77 H. W. Zhang, X. D. Jin, J. M. Lee and X. Wang, *ACS Nano*, 2022, **16**, 17572–17592.
78 W. Y. Song, Y. K. Kang, M. Yang, Z. Li, L. L. Chen, Z. Zhao and J. Liu, *Fuel*, 2022, **311**, 122580.
79 Y. B. Cao, X. Y. Qi, K. H. Hu, Y. Wang, Z. G. Gan, Y. Li, G. R. Hu, Z. D. Peng and K. Du, *ACS Appl. Mater. Interfaces*, 2018, **10**, 18270–18280.
80 C. Zhou, M. Li, N. T. Hu, J. H. Yang, H. Li, J. W. Yan, P. Y. Lei, Y. P. Zhuang and S. W. Guo, *Adv. Funct. Mater.*, 2022, **32**, 2204635.
81 X. C. You, Z. Y. Guo, Q. L. Jiang, J. K. Xia, S. W. Wang, X. H. Yang, Z. C. Zhuang, Y. F. Li, H. Xiang, H. Li and B. Yu, *Nano Lett.*, 2025, **25**, 8704–8712.
82 Z. S. Lu, S. J. Meng, Y. D. Pang, G. L. Xu, D. W. Ma, S. H. Talib and Z. X. Yang, *Phys. B*, 2022, **638**, 413934.
83 J. Wu and Y. X. Yu, *J. Phys. Chem. C*, 2021, **125**, 23699–23708.
84 B. F. Zeng, G. Wang, Q. Z. Qian, Z. X. Chen, X. G. Zhang, Z. X. Lu, S. Q. Zhao, A. N. Feng, J. Shi, Y. Yang and W. J. Hong, *Small*, 2020, **16**, 2004720.
85 H. Q. Ji, M. F. Wang, S. S. Liu, H. Sun, J. Liu, T. Qian and C. L. Yan, *Energy Storage Mater.*, 2020, **27**, 226–231.
86 J. Y. Zhao, J. Lian, Z. X. Zhao, X. M. Wang and J. J. Zhang, *Nano-Micro Lett.*, 2023, **15**, 19.
87 G. N. Qian, S. Kuppan, A. Gallo, J. G. Zhou, Z. Liu and Y. J. Liu, *Energy Storage Mater.*, 2024, **73**, 103819.

88 Z. W. Zhao, X. Zhang, Z. Zhou, E. K. Wang and Z. Q. Peng, *Nano Lett.*, 2022, **22**, 501–507.
89 J. Y. Han, J. R. Sun, S. Y. Chen, S. Y. Zhang, L. L. Qi, A. Husile and J. Q. Guan, *Adv. Mater.*, 2024, **36**, 2408139.
90 L. L. Lyu, X. Hu, S. Lee, W. Q. Fan, G. Kim, J. L. Zhang, Z. Zhou and Y. M. Kang, *J. Am. Chem. Soc.*, 2024, **146**, 4803–4813.
91 Q. Xia, Y. J. Zhai, L. L. Zhao, J. Wang, D. Y. Li, L. L. Zhang and J. T. Zhang, *Energy Mater.*, 2022, **2**, 200015.
92 N. S. Xu, R. Xie, X. H. Yang, R. Xiong, C. L. Wen and B. S. Sa, *Appl. Surf. Sci.*, 2026, **715**, 164414.
93 M. Y. Huang, K. S. Hui, Q. C. Liu, F. M. Chen, S. Sangaraju and K. N. Hui, *EES Batteries*, 2025, **1**, 744–773.
94 X. H. Zou, M. C. Tang, Q. Lu, Y. Wang, Z. P. Shao and L. An, *Energy Environ. Sci.*, 2024, **17**, 386–424.
95 L. S. Peng, L. Shang, T. R. Zhang and G. I. N. Waterhouse, *Adv. Energy Mater.*, 2020, **10**, 2003018.
96 W. W. Zhang, M. L. Wang, H. Zhang, X. L. Huang, B. Y. Shen, B. Song, L. Fu and K. Lu, *Angew. Chem., Int. Ed.*, 2024, **63**, e202317776.
97 C. Yuan, X. C. Song, P. Zeng, G. L. Liu, S. H. Zhou, G. Zhao, H. T. Li, T. R. Yan, J. Mao, H. Yang, T. Cheng, J. P. Wu and L. Zhang, *Nano Energy*, 2023, **110**, 108353.
98 H. F. Gu, W. C. Yue, J. Q. Hu, X. F. Niu, H. Tang, F. J. Qin, Y. Li, Q. Yan, X. M. Liu, W. J. Xu, Z. Y. Sun, Q. Q. Liu, W. S. Yan, L. R. Zheng, Y. Wang, H. Wang, X. Y. Li, L. Zhang, G. M. Xia and W. X. Chen, *Adv. Energy Mater.*, 2023, **13**, 2204014.
99 K. Liu, X. Y. Wang, S. Gu, H. M. Yuan, F. Jiang, Y. Z. Li, W. Tan, Q. R. Long, J. J. Chen, Z. H. Xu and Z. G. Lu, *Small*, 2022, **18**, 2204707.
100 L. Shen, Y. W. Song, J. Wang, C. X. Zhao, C. X. Bi, S. Y. Sun, X. Q. Zhang, B. Q. Li and Q. Zhang, *Small Struct.*, 2023, **4**, 2200205.
101 Y. R. Yan, N. Fu, W. Shao, T. T. Wang, Y. Liu, Y. S. Niu, Y. W. Zhang, M. Peng and Z. L. Yang, *Small*, 2024, **20**, 2311799.
102 X. Y. Lin, W. Y. Li, V. Nguyen, S. Wang, S. Z. Yang, L. Ma, Y. H. Du, B. Wang and Z. Y. Fan, *Chem. Eng. J.*, 2023, **477**, 146977.
103 Q. J. Shao, L. Xu, D. C. Guo, Y. Su and J. Chen, *J. Mater. Chem. A*, 2020, **8**, 23772.
104 Y. F. Ding, Q. S. Cheng, J. H. Wu, T. R. Yan, Z. X. Shi, M. L. Wang, D. Z. Yang, P. Wang, L. Zhang and J. Y. Sun, *Adv. Mater.*, 2022, **34**, 2202256.
105 H. Sun, X. Li, T. Q. Chen, S. X. Xia, T. Yuan, J. H. Yang, Y. P. Pang and S. Y. Zheng, *ACS Appl. Mater. Interfaces*, 2023, **15**, 19043.
106 R. Wang, J. L. Qin, F. Pei, Z. Z. Li, P. Xiao, Y. H. Huang, L. X. Yuan and D. L. Wang, *Adv. Funct. Mater.*, 2023, **33**, 2305991.
107 Y. J. Li, S. Y. Lin, D. D. Wang, T. T. Gao, J. W. Song, P. Zhou, Z. K. Xu, Z. H. Yang, N. Xiao and S. J. Guo, *Adv. Mater.*, 2020, **32**, 1906722.
108 C. L. Song, Z. H. Li, L. Y. Ma, M. Z. Li, S. Huang, X. J. Hong, Y. P. Cai and Y. Q. Lan, *ACS Nano*, 2021, **15**, 13436–13443.
109 T. Huang, Y. J. Sun, J. H. Wu, J. Jin, C. H. Wei, Z. X. Shi, M. L. Wang, J. S. Cai, X. T. An, P. Wang, C. L. Su, Y. Y. Li and J. Y. Sun, *ACS Nano*, 2021, **15**, 14105–14115.
110 Y. J. Li, T. T. Gao, D. Y. Ni, Y. Zhou, M. Yousaf, Z. Q. Guo, J. H. Zhou, P. Zhou, Q. Wang and S. J. Guo, *Adv. Mater.*, 2022, **34**, 2107638.
111 C. X. Bi, N. Yao, X. Y. Li, Q. K. Zhang, X. Chen, X. Q. Zhang, B. Q. Li and J. Q. Huang, *Adv. Mater.*, 2024, **36**, 2411197.
112 Y. F. Wang, C. L. Xu, B. B. Li, M. Tian, M. Liu, D. M. Zhu, S. X. Dou, Q. Zhang and J. Y. Sun, *ACS Nano*, 2024, **18**, 34858–34869.
113 H. Y. Wu, X. J. Gao, X. Y. Chen, W. H. Li, J. J. Li, L. Zhang, Y. Zhao, M. Jiang, R. C. Sun and X. L. Sun, *Carbon Energy*, 2024, **6**, e422.
114 Y. H. Lin, J. Wang, X. Zhang, X. M. Cheng, Q. Zhuang, J. Zhang, Q. H. Guan, Y. L. Wang, C. Y. Shen, H. Z. Lin, L. Zhan, L. C. Ling and Y. Z. Zhang, *Adv. Funct. Mater.*, 2025, 2501496.
115 X. M. Zhang, T. Z. Yang, Y. G. Zhang, X. B. Wang, J. Y. Wang, Y. B. Li, A. P. Yu, X. Wang and Z. W. Chen, *Adv. Mater.*, 2023, **35**, 2208470.
116 H. Tian, H. J. Tian, S. J. Wang, S. M. Chen, F. Zhang, L. Song, H. Liu, J. Liu and G. X. Wang, *Nat. Commun.*, 2020, **11**, 5025.
117 C. G. Wang, H. W. Song, C. C. Yu, Z. Ullah, Z. X. Guan, R. R. Chu, Y. F. Zhang, L. Y. Zhao, Q. Li and L. W. Liu, *J. Mater. Chem. A*, 2020, **8**, 3421–3430.
118 Y. Z. Song, L. W. Zou, C. H. Wei, Y. Zhou and Y. Hu, *Carbon Energy*, 2023, **5**, e286.
119 B. W. Zhang, T. Sheng, Y. X. Wang, S. Chou, K. Davey, S. X. Dou and S. Z. Qiao, *Angew. Chem., Int. Ed.*, 2019, **58**, 1484–1488.
120 P. Wang, B. J. Xi, Z. C. Y. Zhang, M. Huang, J. K. Feng and S. L. Xiong, *Angew. Chem., Int. Ed.*, 2021, **60**, 15563–15571.
121 P. Xiong, F. Zhang, X. Y. Zhang, S. J. Wang, H. Liu, B. Sun, J. Q. Zhang, Y. Sun, R. Z. Ma, Y. Bando, C. F. Zhou, Z. W. Liu, T. Sasaki and G. X. Wang, *Nat. Commun.*, 2020, **11**, 3297.
122 X. Zhong, Y. J. Huang, J. M. Cai, Y. J. Li, Z. D. He, D. Y. Cai, Z. L. Geng, W. T. Deng, G. Q. Zou, H. S. Hou and X. B. Ji, *J. Am. Chem. Soc.*, 2024, **146**, 32124–32134.
123 N. C. Lai, G. Conga and Y. C. Lu, *J. Mater. Chem. A*, 2019, **7**, 20584–20589.
124 W. Q. Song, X. Y. Yang, T. Zhang, Z. C. Huang, H. Z. Wang, J. Sun, Y. H. Xu, J. Ding and W. B. Hu, *Nat. Commun.*, 2024, **15**, 1005.
125 B. W. Zhang, T. Sheng, Y. D. Liu, Y. X. Wang, L. Zhang, W. H. Lai, L. Wang, J. Yang, Q. F. Gu, S. L. Chou, H. K. Liu and S. X. Dou, *Nat. Commun.*, 2018, **9**, 4082.
126 X. L. Ge, H. X. Di, P. Wang, X. G. Miao, P. Zhang, H. Y. Wang, J. Y. Ma and L. W. Yin, *ACS Nano*, 2020, **14**, 16022–16035.
127 J. Zheng, Y. Yang, X. L. Fan, G. B. Ji, X. Ji, H. Y. Wang, S. Hou, M. R. Zachariah and C. S. Wang, *Energy Environ. Sci.*, 2019, **12**, 615–623.
128 E. H. Zhang, X. Hu, L. Z. Meng, M. Qiu, J. X. Chen, Y. J. Liu, G. Y. Liu, Z. C. Zhuang, X. B. Zheng, L. R. Zheng, Y. Wang,

W. Tang, Z. G. Lu, J. T. Zhang, Z. H. Wen, D. S. Wang and Y. D. Li, *J. Am. Chem. Soc.*, 2022, **144**, 18995–19007.
129 Y. J. Lei, X. X. Lu, H. Yoshikawa, D. Matsumura, Y. M. Fan, L. F. Zhao, J. Y. Li, S. J. Wang, Q. F. Gu, H. K. Liu, S. X. Dou, S. Devaraj, T. Rojo, W. H. Lai, M. Armand, Y. X. Wang and G. X. Wang, *Nat. Commun.*, 2024, **15**, 3325.
130 W. Q. Song, Z. Z. Wen, X. Wang, K. Y. Qian, T. Zhang, H. Z. Wang, J. Ding and W. B. Hu, *Nat. Commun.*, 2025, **16**, 2795.
131 T. T. Luo, Y. Wang, B. Elander, M. Goldstein, Y. Mu, J. Wilkes, M. Fahrenbruch, J. Lee, T. Li, J. L. Bao, U. Mohanty and D. W. Wang, *Adv. Mater.*, 2024, **36**, 2306239.
132 W. Z. Kou, Z. T. Fang, H. Z. Ding, W. Luo, C. Liu, L. M. Peng, X. F. Guo, W. P. Ding and W. H. Hou, *Adv. Funct. Mater.*, 2024, **34**, 2406423.
133 X. Q. Sun, P. Bonnick and L. F. Nazar, *ACS Energy Lett.*, 2016, **1**, 297–301.
134 Q. N. Zhao, R. H. Wang, Y. X. Zhang, G. S. Huang, B. Jiang, C. H. Xu and F. S. Pan, *J. Magnesium Alloys*, 2021, **9**, 78–89.
135 F. P. Xiao, H. K. Wang, J. Xu, W. Q. Yang, X. M. Yang, D. Y. W. Yu and A. L. Rogach, *Adv. Energy Mater.*, 2021, **11**, 2100989.
136 Y. Xu, Y. F. Ye, S. Y. Zhao, J. Feng, J. Li, H. Chen, A. K. Yang, F. F. Shi, L. J. Jia, Y. Wu, X. Y. Yu, P. A. Glans-Suzuki, Y. Cui, J. H. Guo and Y. G. Zhang, *Nano Lett.*, 2019, **19**, 2928–2934.
137 Z. R. Zhao-Karger, X. Y. Zhao, D. Wang, T. Diemant, R. J. Behm and M. Fichtner, *Adv. Energy Mater.*, 2015, **5**, 1401155.
138 T. X. Zou, T. Xu, S. L. Ju and X. B. Yu, *Chem. Eng. J.*, 2023, **477**, 147207.
139 Q. H. Guan, J. Wang, Q. Zhuang, J. Zhang, L. G. Li, L. J. Jia, Y. Z. Zhang, H. F. Hu, H. M. Hu, S. Cheng, H. Zhang, H. H. Li, M. N. Liu, S. Y. Wang and H. Z. Lin, *Energy Environ. Sci.*, 2024, **17**, 3765.
140 S. L. Ju, C. Y. Yuan, J. N. Zheng, L. Yao, T. F. Zhang, G. L. Xia and X. B. Yu, *Energy Storage Mater.*, 2022, **52**, 524–533.
141 X. F. Yang, J. Luo and X. L. Sun, *Chem. Soc. Rev.*, 2020, **49**, 2140–2195.
142 H. T. Yang, Y. H. Xu, Y. F. Zhao, C. N. Geng, H. L. Ge, L. Wang, W. Lv, C. P. Yang, W. Chen and Q. H. Yang, *Adv. Funct. Mater.*, 2025, **35**, 2426089.
143 Z. Y. Wang, H. L. Ge, S. Liu, G. R. Li and X. P. Gao, *Energy Environ. Mater.*, 2023, **6**, e12358.
144 Y. H. Xu, W. C. Yuan, C. N. Geng, Z. H. Hu, Q. Li, Y. F. Zhao, X. Zhang, Z. Zhou, C. P. Yang and Q. H. Yang, *Adv. Sci.*, 2024, **11**, 2402497.
145 Z. X. Chen, Q. Cheng, X. Y. Li, Z. Li, Y. W. Song, F. R. Sun, M. Zhao, X. Q. Zhang, B. Q. Li and J. Q. Huang, *J. Am. Chem. Soc.*, 2023, **145**, 16449–16457.
146 Z. X. Chen, J. J. Zhao, G. Y. Fang, F. R. Sun, M. Zhao, X. Q. Zhang, B. Q. Li and J. Q. Huang, *J. Energy Chem.*, 2025, **109**, 129–137.
147 H. T. Yang, L. Wang, C. N. Geng, Y. F. Zhao, Q. Li, X. Jiang, Z. L. Tian, M. Wang, C. L. Jiang, Z. J. Sun, B. H. Cui, Y. B. He, W. Chen, W. Lv and Q. H. Yang, *Adv. Energy Mater.*, 2024, **14**, 2400249.
148 M. He, Y. X. Fan, S. Liu, S. Y. Wang, T. W. Wu, D. J. Chen, A. J. Hu, C. Y. Yan, Y. C. Yan, J. P. Long, Y. Hu, T. Y. Lei, P. Li and W. Chen, *Adv. Energy Mater.*, 2025, **15**, 2405642.
149 X. Y. Li, S. Feng, Y. W. Song, C. X. Zhao, Z. Li, Z. X. Chen, Q. Cheng, X. Chen, X. Q. Zhang, B. Q. Li, J. Q. Huang and Q. Zhang, *J. Am. Chem. Soc.*, 2024, **146**, 14754–14764.
150 X. Y. Li, B. Q. Li, S. Feng, Z. Li, L. Shen, S. Y. Sun, Z. X. Chen, T. Jin, X. Chen, M. Zhao, X. Q. Zhang, J. Q. Huang and Q. Zhang, *J. Am. Chem. Soc.*, 2025, **147**, 15435–15447.
151 Z. X. Chen, J. J. Zhao, G. Y. Fang, S. Zhang, J. Ma, M. Zhao, B. Q. Li and J. Q. Huang, *Energy Storage Mater.*, 2025, 104502.
152 E. I. Andritsos, C. Lekakou and Q. Cai, *J. Phys. Chem. C*, 2021, **125**, 18108–18118.
153 B. B. Gicha, L. T. Tufa, N. Nwaji, X. J. Hu and J. Lee, *Nano-Micro Lett.*, 2024, **16**, 172.
154 Y. W. Song, L. Shen, X. Y. Li, C. X. Zhao, J. Zhou, B. Q. Li, J. Q. Huang and Q. Zhang, *Nat. Chem. Eng.*, 2024, **1**, 588–596.
155 Z. Lian, M. Yang, F. Jan and B. Li, *J. Phys. Chem. Lett.*, 2021, **12**, 7053–7059.